



Local buckling on large sandwich panels applied to light aviation: Experimental and computation dialogue

M. Ginot, C. Bouvet, B. Castanié, M. d'Ottavio, Joël Serra, N. Mahuet

► To cite this version:

M. Ginot, C. Bouvet, B. Castanié, M. d'Ottavio, Joël Serra, et al.. Local buckling on large sandwich panels applied to light aviation: Experimental and computation dialogue. International Journal of Solids and Structures, 2023, 268, pp.112170. 10.1016/j.ijsolstr.2023.112170 . hal-04080624

HAL Id: hal-04080624

<https://hal.science/hal-04080624>

Submitted on 25 Apr 2023

HAL is a multi-disciplinary open access archive for the deposit and dissemination of scientific research documents, whether they are published or not. The documents may come from teaching and research institutions in France or abroad, or from public or private research centers.

L'archive ouverte pluridisciplinaire **HAL**, est destinée au dépôt et à la diffusion de documents scientifiques de niveau recherche, publiés ou non, émanant des établissements d'enseignement et de recherche français ou étrangers, des laboratoires publics ou privés.

Local buckling on large sandwich panels applied to light aviation:

Experimental and computation dialogue.

M. Ginot^{a,b}, C. Bouvet^b, B. Castanié^{b,*}, M. D'Ottavio^c, J. Serra^b, N. Mahuet^a

^a Elixir Aircraft, Rue du Jura, 17000 La Rochelle, France

^b Institut Clément Ader (ICA), Université de Toulouse, CNRS UMR 5312, INSA, ISAE-Supaéro, INSA, IMT Mines Albi, UPS, Toulouse, France

^c LEME – EA4416, Université Paris Nanterre, 50, Rue de Sèvres, 92410 Ville d'Avray, France

* Corresponding author: bruno.castanie@insa-toulouse.fr

Keywords: Sandwich structures; Local buckling; Wrinkling; Structural testing; Experimental and computation dialogue; nonlinear FEM.

Abstract

Wrinkling is a local buckling phenomenon in sandwich structures subjected to compression and shear loading **that** is challenging for the **aircraft** design engineer. Numerous wrinkling models are proposed in the literature **but** historical formulas developed after the Second World War are **still widely used by the industry with important knock down factors**. Theory-experiment correlation should be the final step in validating and evaluating the models. This article **presents an experimental-computational dialogue** on structural tests on large sandwich panels of dimensions 558 x 536 mm² representative of the design used in light aviation. The panels were subjected to compressive and shear loading by using the VERTEX test bench and wrinkling failures were observed. Comparisons are first made with linear

wrinkling models. Despite correlations are quite encouraging, the imperfection-sensitivity of the experimentally observed wrinkling failure questions the pertinence of a linear bifurcation approach. A nonlinear Finite Element Model (FEM) of the sandwich panels is then developed. Initial imperfections measured by Stereo Digital Image Correlation (SDIC) are directly introduced in the mesh and an elastoplastic constitutive law for the core is implemented. Dynamic explicit computation is used to access the highly nonlinear ~~post-buckling~~ behaviour and matches the test observations very well. The nonlinear FEM provides an improved, conservative prediction of wrinkling loads over the linear models.

1 Introduction

Wrinkling is a local instability that can occur when a sandwich structure is subjected to compression or shear loading. The length of the wrinkle pattern is of the order **of magnitude** of the thickness of the sandwich. Wrinkling is considered a primary cause of failure in sandwich structures with thin skins and low core characteristics, such as the configurations used in light aviation. Wrinkling models have been under development since the Second World War and several literature reviews retrace the evolution of wrinkling modelling (Castanié et al., 2020; Ley et al., 1999; Ginot et al., 2021). Without being exhaustive, the first historical formulas were developed with hypotheses using isotropic skins on an elastic foundation in a 2D framework (Hoff and Mautner, 1945; Plantema, 1966; Allen, 1969). More recent works achieved unified models capable of describing global and local buckling modes in sandwich structures (Benson and Mayers, 1967; Leotoing, 2001; Niu and Talreja, 1999; Douville and Le Grogne, 2013). Other models have been enriched by adding orthotropy for the skin (Fagerberg and Zenkert, 2005a) and for the core (Vonach and Rammerstorfer, 2000) and the possibility of a multiaxial

loading (Sullins et al., 1969; Birman and Bert, 2004). **Eventually, few** authors have proposed higher order formulations with numerical resolutions. An interesting approach is the Sublamine Generalised Unified Formulation (S.G.U.F) developed by D'Ottavio (2016). Based on a variable kinematic approach, the formulation allows dedicated models to be introduced for skins and core, thus allowing to choose and identify the model required for properly grasping global and/or local response depending on the problem considered (D'Ottavio et al., 2016; Vescovini et al., 2018). To a lesser extent in the literature, **experimental-computational dialogues** on sandwich structures have been achieved. Thomsen et al. (1996a; 1996b) worked on the influence of the ply drops on sandwich beams with honeycomb core from an enhanced Winkler model. Out-of-plane skin displacement has been solved numerically. Fagerberg (2004; Fagerberg and Zenker 2005a) carried out important test campaigns on sandwich panels, and his results have been used as a reference for the validation of several wrinkling models (Fagerberg and Zenkert, 2005a; Fagerberg and Zenkert, 2005b). At the structure scale, Tuwair et al. (2016) conducted a test on a sandwich panel under four point bending. Correlations were performed with finite-element analyses and analytical models. Tuwair et al. (2016) noted that using analytical approaches to find an exact solution for wrinkling problems may be limited by the assumptions adopted for these methods. This remark is far from new. After a test campaign, Hoff and Mautner (1945) recommended a knock down factor for their analytical solution. This was taken up by Zenkert's sandwich construction handbook (1997) and NASA's technical documents of the late 1960s (Sullins et al., 1969). Most of the experimental results on wrinkling show that the classical formulas provide correct trends but with a non-conservative load prediction (Hoff and Mautner, 1945; Norris, 1964). Therefore, the aeronautic industry often uses the knock down factor recommended by Hoff and Mautner

to cover this complex phenomenon. The main reason why the analytical expressions are not conservative is that the initial imperfections and displacements before buckling are not considered. **The quantification of the effect of these imperfections is difficult especially in the structural cases presented in this study. According to Fagerberg and Zenkert (2005a), in the case of non-negligible imperfections (with an amplitude of the order of magnitude of $1/10^{\text{th}}$ of the face sheet thickness), the out-of-plane displacement before buckling will be significant and will increase significantly the non-linear behaviour of the structure.** Therefore, Finite Element Models (FEM) often provide a more accurate way of taking geometric and/or mechanical non-linearity into account and investigating the post-wrinkling behaviour.

Several approaches can be followed to model a sandwich structure by commercial FE packages. The use of an equivalent single layer model by means of shell elements with a composite section is the less expensive approach but it is inapplicable for wrinkling studies because it discards the out-of-plane deformation of the core. A three-layer model should thus be adopted, where the core is modelled by continuum elements in order to retain its out-of-plane response required for wrinkling analysis. The skins may be modelled by shell elements or by continuum elements, the former approach being computationally more advantageous due to the thinness of the skins, which would require too small continuum elements for avoiding excessive element aspect ratios (Léotoing et al., 2002). Convergence studies performed by Léotoing et al. (2002) also recommended to use a mesh density such that each wavelength of the wrinkling pattern is discretized by at least 8 linear elements. **For this matter, a preliminary analytical computation of the expected wavelength is of great help to select a first mesh density.**

In the literature, models are too often compared to textbook cases – either directly via finite element models, with no geometric defects and perfect boundary conditions (Ginot et al., 2021), or via coupon scale tests that are simple to implement but suffer from underlying boundary condition problems (Ley et al., 1999). A preceeding paper (Ginot et al., 2023) on the subject presents wrinkling tests under multiaxial stresses at the plate scale. Five sandwich panels were tested under compressive and shear loading with the VERTEX test bench (Figure 1) and wrinkling type failure was observed. The sandwich panel configurations were chosen to be consistent with the sandwich structures used in light aviation (Castanié et al., 2020; Elixir Aircraft). The VERTEX test bench (Figure 1) develops boundary conditions representative of what an aeronautic sandwich panel can undergo in real conditions (Serra et al., 2017a). **This experimental campaign provided a large number of valuable data concerning wrinkling of built-up structures. The present paper thus presents an original and enhanced dialogue between experimental testing and computational modelling; the novelty resides in the consideration of the wrinkling phenomenon at the structural scale within an industry-oriented context related to light aviation, which allows to shed light on various aspects influencing this critical failure mode.**

The paper is organized as follows. **First**, the material, methods and results of the VERTEX test campaign discussed in (Ginot et al., 2023) are summarised for presenting a self-contained paper. Subsequently, the **experimental-computational dialogue** is presented in two main parts: (1) Comparisons are made with linear wrinkling models, results and limits being discussed, and (2) an advanced FEM is developed and the nonlinear analysis is compared to the test results. **Eventually**, conclusions are drawn.

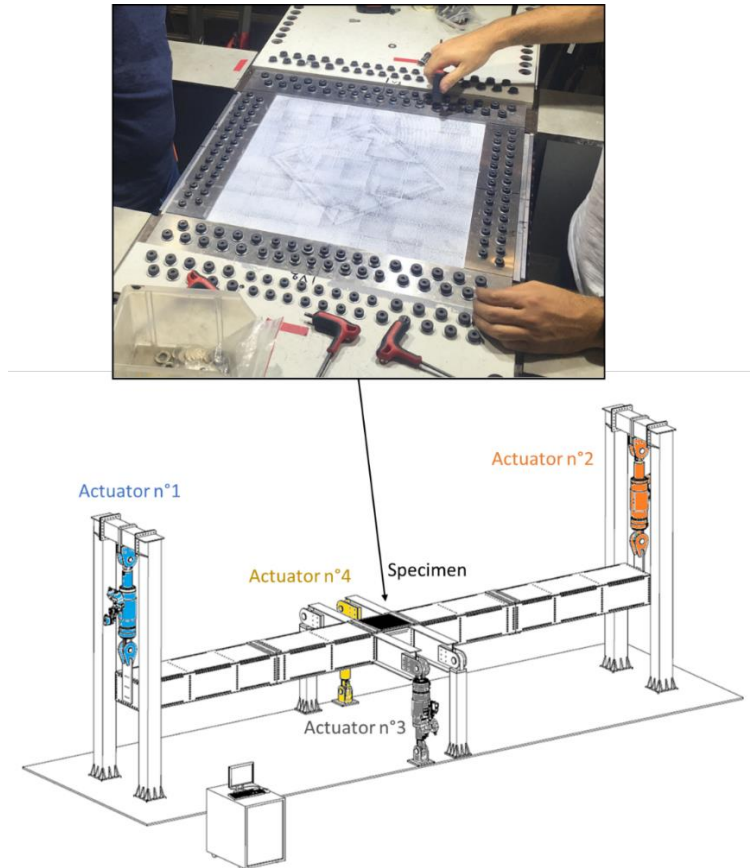


Figure 1: VERTEX test bench and details of a specimen bolted onto the upper part of the central box.

2 Materials, method, and test results

2.1 Materials and method

The operating principle of the VERTEX machine involves four hydraulic actuators used to load a rectangular box structure. The panel under test closes the upper part of the central box (Figure 1). Actuators 1 and 2 can push or pull symmetrically to bend the box structure of the bench, thus locally loading the tested panel in tension or compression. Similarly, actuators 3 and 4 can push to twist the centre of the box structure, thus locally loading the tested panel in shear. The specimens used here were sandwich panels with a monolithic peripheral area and an asymmetric sandwich central area including a tapered region. As a result, the edges were monolithic and were drilled to bolt the specimen to the VERTEX test bench (Figure 2).

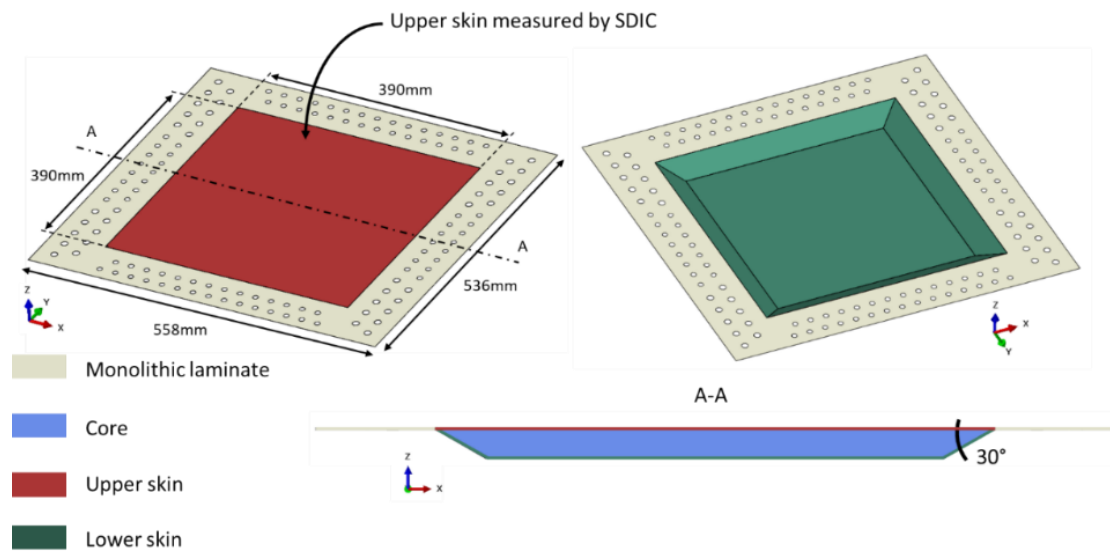


Figure 2: Overall panel geometry.

The specimen was positioned as shown in Figure 1 and bolted on its 4 sides with 128 screws. The external dimensions were 558 x 536 mm², and the sandwich area with the tapered regions was 390 x 390 mm² and about 21 mm thick (core and skins). The materials used for the specimens were a Polymethacrylimide (PMI) foam of density 51 kg/m³ and prepreg carbon/epoxy woven fabric with additional unidirectional prepreg in the F51_D2 sandwich configuration. The nominal stacking sequences are shown in Table 1. A "one-shot/co-cured" process was used in an autoclave. **Specimens** were tested under **either** compressive **loading** or shear **loading** (Ginot et al., 2023). Three of the five specimens tested in (Ginot et al., 2023) are studied in the present paper.

The observable surface was the upper skin; the lower skin faced the inner test bench box structure. To locate wrinkling in the upper skin, an asymmetric geometry was used to create an offset between the load introduction axis and the mean geometric plane of the sandwich structure. It led to a bending moment and induced an additional compressive load in the upper skin and a tensile load in the lower skin. The upper skin was thus more loaded and was liable to buckle.

Table 1: Specimen stacking sequence in nominal area. Specimen nomenclature is F51_... for 51 kg/m³ PMI foam and ..._Dx for specified stacking sequence.

Specimen	F51_D1	F51_D2	F51_D3
Loading	Compressive	Compressive	Shear
Stacking sequence	Fabric +/- 45°	Fabric +/- 45°	Fabric +/- 45°
		2x Unidir 0°	
	Fabric 0°/90°	Fabric 0°/90°	Fabric +/- 45°
	PMI foam	PMI foam	PMI foam
	Fabric 0°/90°	Fabric 0°/90°	Fabric +/- 45°
	Fabric +/- 45°	Fabric +/- 45°	Fabric +/- 45°
			Fabric +/- 45°

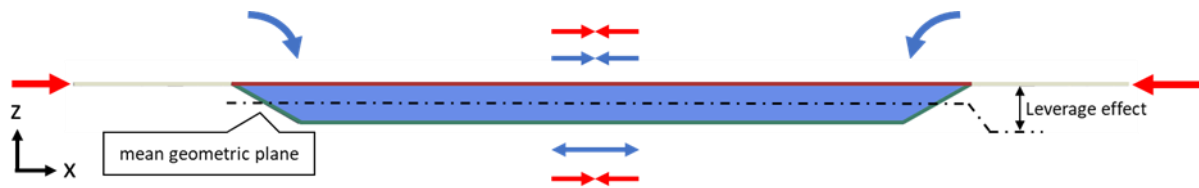


Figure 3: Bending effect on asymmetric sandwich structure.

To locate the wrinkling in the centre of the panel, a high-density foam frame was used to reinforce the tapered area. For the specimen under compressive loads, the nominal area was 260 x 260 mm² (dotted frames in Figure 4 (a) and (b)).

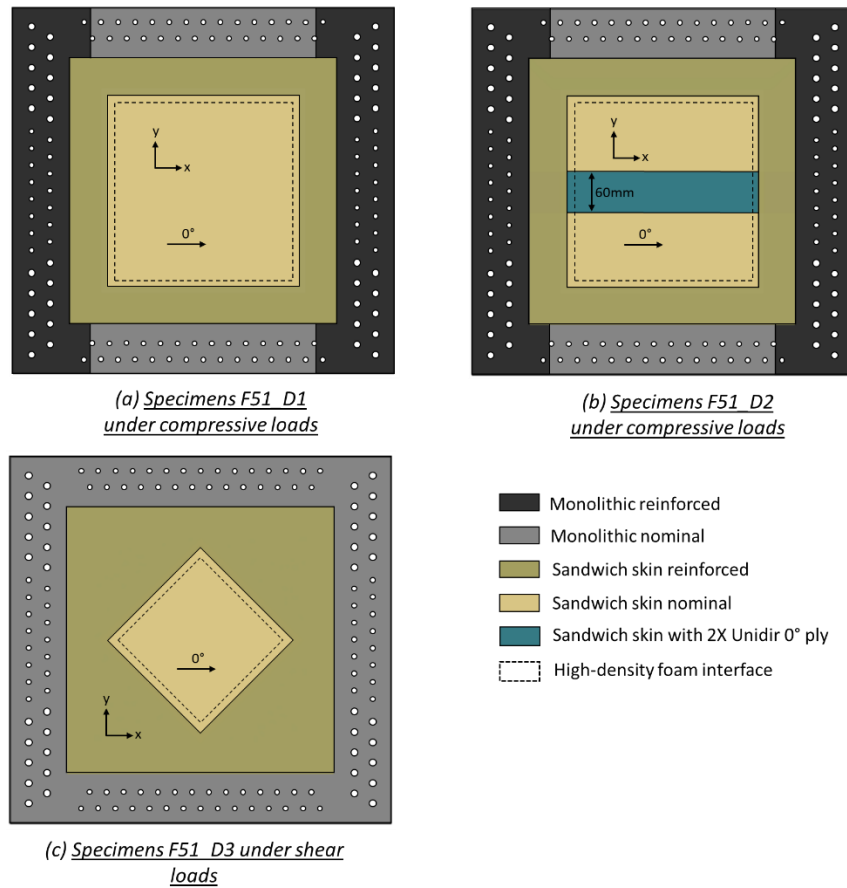


Figure 4: Skin definition of the specimens.

Skins in the tapered area were reinforced (dark brown area in Figure 4). For the specimen under shear loads, the nominal area (dotted frame in Figure 4 (c)) had a 172 x 172 mm² **diamond** shape so as to have edges perpendicular to the principal stresses at $\pm 45^\circ$. For specimen F51_D2, a 60 mm wide strip of 2X Unidirectional plies 0° ply was added (blue area in Figure 4 (b)) as a typical stacking used in light aviation. The area where the stacking sequence corresponded to Table 1 was called the “nominal area” (light brown inside the dotted frame area in Figure 4 (a) and (c) for specimens F51_D1 and F51_D3; blue area in Figure 4 (b) for specimens F51_D2).

2.2 Instrumentation

Stereo Digital Image Correlation (SDIC) with two 5 Mpx cameras was used, and a speckled pattern was made on the upper face of the specimens (Figure 5 (a)). The acquisition frequency was set to two images per second. Vic3D software (Correlated Solutions Inc., Columbia, SC, USA) was used for post-processing. A high-speed camera (7000 fps) was **also** used to observe a potential explosive failure (Figure 5 (b)). **An infrared camera was added** to the setup (Figure 5 (c)), allowing for possible wrinkling type failure measurements. In the lower skin, “Rosette” gauges were used (the location of the gauges can be found in Ginot et al, 2023, figure 12).

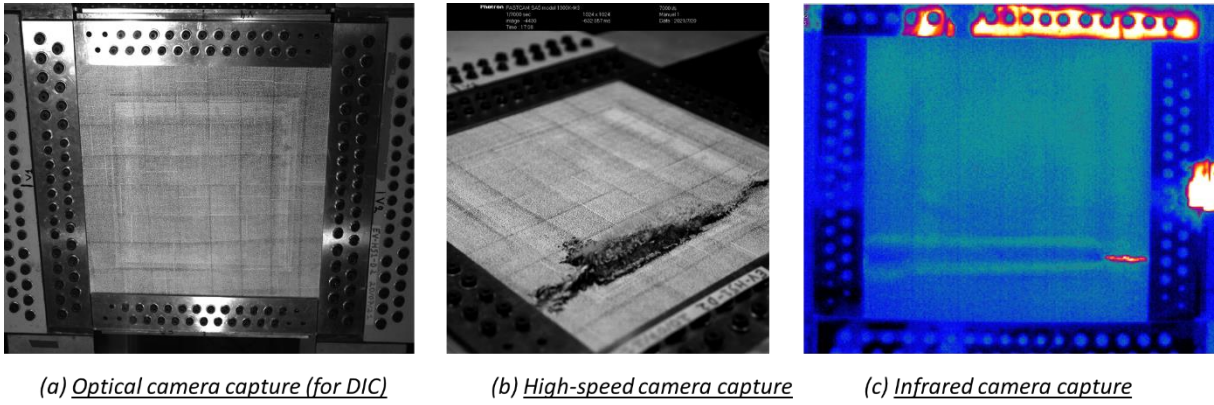


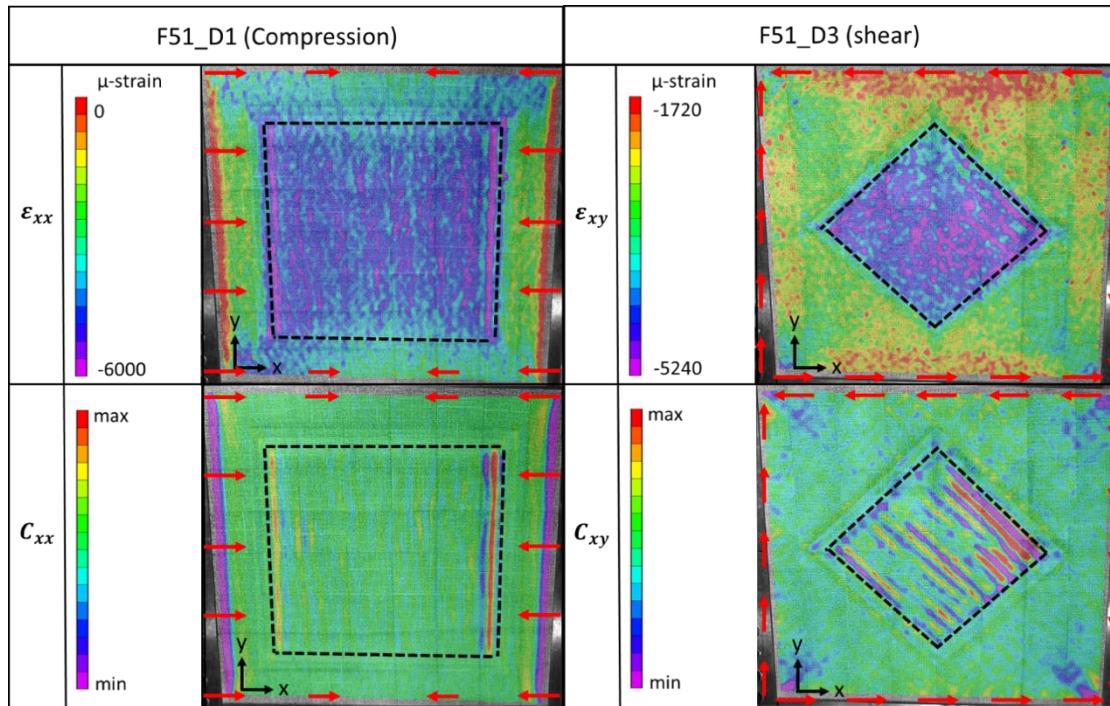
Figure 5: Images captured by instrumentation cameras.

2.3 Results

2.3.1 Strain and curvature fields

Figure 6 shows in-plane strains (ϵ_{xx} field of F51_D1 and ϵ_{xy} field of F51_D3). All the frames were taken just before failure. A post-treatment is carried out in order to avoid the grained noise characterizing the SDIC recordings in view of a clearer observation of the wrinkling waves, see (Ginot et al, 2023) for more details. The waves of the wrinkling state do not appear clearly and the whole plate remains under compression or shear respectively. The strains are mainly uniform and follow typical expectations. Therefore, the curvature fields,

i.e. the inverse diameter of the circle locally tangent to the out-of-plane displacement are also shown Figure 6 (C_{xx} field of F51_D1 and C_{xy} field of F51_D3). The waves appear more clearly and are located near the boundaries of the central area for the compression case; For the shear case, waves are extensively present in the whole area of interest, but larger amplitudes are located near the boundaries also.



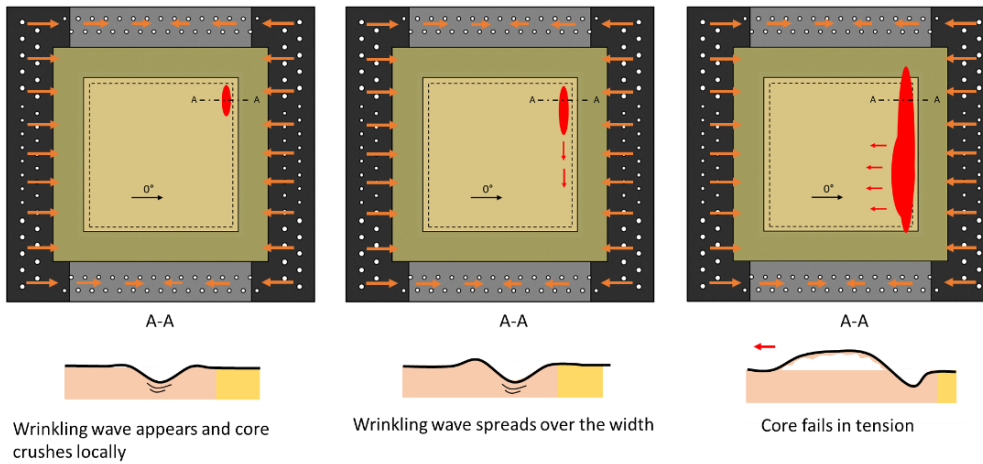
[] Nominal area

Figure 6: Strains and curvatures evolution fields obtained by SDIC just before failure in specimens F51_D1 and F51_D3.

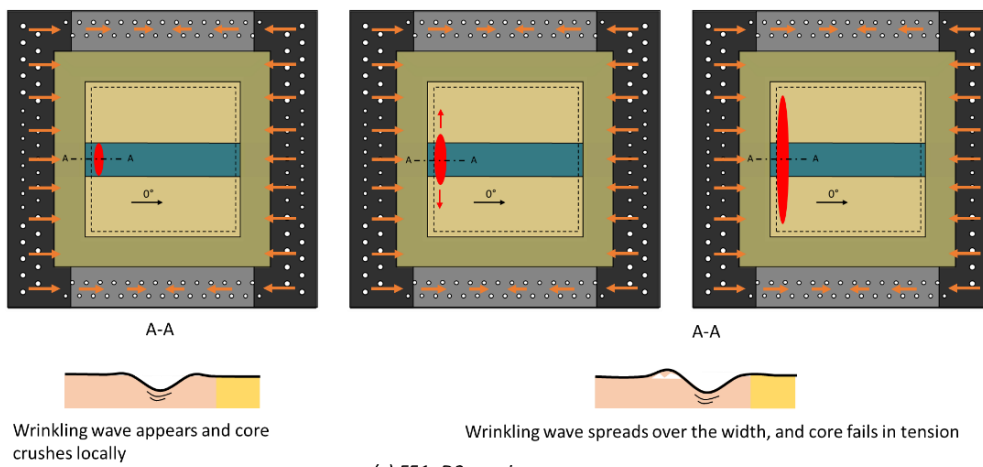
2.3.2 Failure scenario

For most specimens, the failure behaviour was similar (Figure 7). The specimens failed by wrinkling in the upper skin, thus validating the design of the specimens. **One or more wrinkling waves appeared provoking the core to crush locally. The wave eventually spread over the width with a failure of the core due to tension along the thickness direction. This**

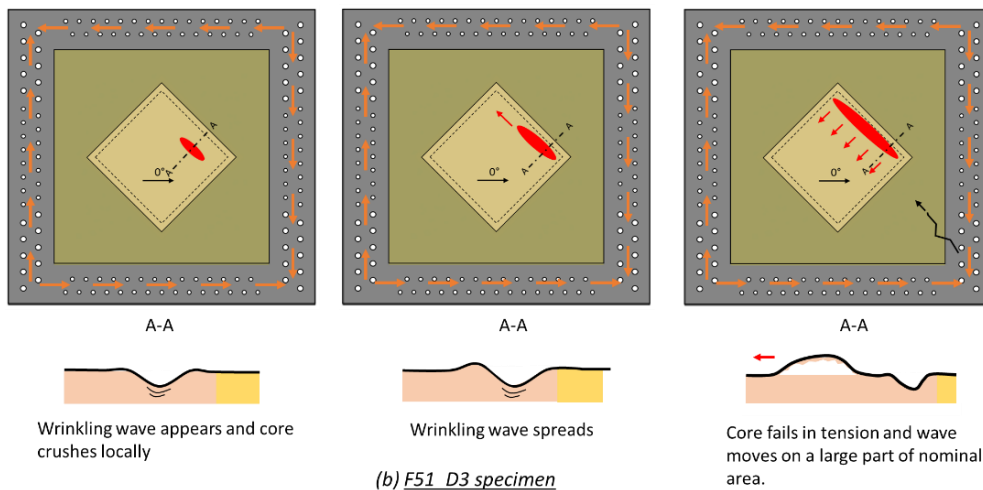
190 lasted about 2 milliseconds starting from the core crushing. For the shear-loaded specimen,
191 the wrinkling wave followed the direction of the compressive principal stress.



(a) *F51_D1 specimen*



(c) *F51_D2 specimen*



(b) *F51_D3 specimen*

Main loading direction
 PMI foam
 High-density foam
 Skin wave
 Skin static failure
 Nominal/High-density foam interface

Figure 7: Failure scenario for specimens F51_D1, F51_D2 and F51_D3.

2.4 Compressive and shear strains at failure

Table 2 lists the average principal compressive direction and compressive strain at failure of **the upper skin of the sandwich panel** in the nominal area for each specimen tested. The average compressive strain at specimen failure is measured thanks to SDIC (numerical extensometer) in the nominal area. For specimens under compressive loading, the principal compressive direction is not more than 4° from the x-axis, **which** can be considered as pure compression. For the specimen under shear loading, the principal compressive direction is about 52° from the x-axis whereas in a pure shear case it should be at 45°. This is due to a tensile component resulting from coupling between torsion and bending in the VERTEX bench. Therefore, the principal strain ε_2 is noted instead of the 45° strain. **Note that more information on the measurement method and parameters, the calculation of the average compressive or shear strains, are available in Ginot et al, 2023.**

Table 2: Average strain at failure.

Specimen	F51_D1	F51_D2	F51_D3
Loading	Compression	Compression	Shear
Failure type	wrinkling	wrinkling	wrinkling
Principal compressive direction	3.9°	3.6°	51.8°
Average compressive strain at failure	$\varepsilon_{xx} = -5400 \mu \text{ strains}$	$\varepsilon_{xx} = -3400 \mu \text{ strains}$	$\varepsilon_2 = -4600 \mu \text{ strains}$

3 Experimental and computation dialogue: Linear bifurcation analysis in a 2D framework

A first try to simulate VERTEX test and the wrinkling phenomena is the use of linear models in a 2D plane strain setting subjected to uniaxial compressive loading. Due to the specific geometry of the panel specimen used in the VERTEX bench (see Figure 3), the sandwich section is not uniformly strained in the axial direction: the upper skin is more loaded and is where the wrinkling instability is of interest, whereas the lower skin carries a lower compressive load due to the overall bending of the specimen. Therefore, it is assumed that the experimentally measured wrinkling pertains to a one-sided mode. Thus, the thickness of the core in the analytical models is chosen to be 50mm, instead of 20mm (the thickness of the VERTEX sandwich specimens), in order to prevent any interactions between the two skins and being comparable to a one-sided mode. Moreover, the same layup is attributed to both skins (symmetric sandwich section) and the skins' thickness and layup is taken to correspond to the upper skin of the VERTEX sandwich panel (Table 1). Finally, since the load introduction is not as simple, it appears more meaningful to compare critical strains of the upper skin rather than critical loads, which also allows a direct comparison with the experimental results reported in Table 2.

3.1 Analytical formulations

A number of analytical wrinkling formulae are considered to evaluate the critical bifurcation load in the two-dimensional, plane strain setting, see also (Ginot et al., 2021). In many cases, the skin stiffness appearing in the formula is expressed by the longitudinal Young's modulus. Since composite laminated skins are studied, this property is computed from the flexural

230 rigidity in the direction of the compressive load as $E_{s\ flex} = \frac{12}{D_{11}^* t_s^3}$ (D^* is the inverse of the
231 bending stiffness matrix of the laminate). We refer to the original works for the details of the
232 models taken from the literature: (Hoff and Mautner, 1945; Niu and Talreja, 1999; Leotoing,
233 2001; Douville and Le Grogneq, 2013). Note that, for Hoff and Mautner’s pioneering formula:
234 $\sigma_{crit} = Q(E_{s\ flex}E_cG_c)^{1/3}$, where E_c and G_c are the core modulus and the core transverse
235 shear modulus, respectively, Q is a constant that has been theoretically calculated at 0.91, but
236 Hoff and Mautner recommend a “practical” constant Q of 0.5 considering that Q plays the
237 role of a knock down factor. Both values are compared with test results.

238 As in (Ginot et al., 2021), new results obtained by a S.G.U.F. model are also reported. In order
239 to refrain from simplifying assumptions that may introduce theory-driven inaccuracies, a high-
240 order kinematics with through-thickness cubic axial displacement and quadratic transverse
241 displacement is used for the composite skins. So, parabolic transverse shear strains as well as
242 a linear thickness-stretch are retained. The model for the core is quasi-3D with the
243 displacements approximated by through-thickness polynomials of 12th order. The initial stress
244 matrix is computed upon uniformly straining the whole sandwich section (i.e., the core carries
245 a certain amount of initial compressive load also) and by referring to von Kármán non-
246 linearities. A Navier-type solution is adopted for defining the longitudinal periodic pattern,
247 see, e.g., (D’Ottavio and Polit, 2015; D’Ottavio et al., 2016). Since the wavelength of the
248 wrinkling pattern is an input, the actual wrinkling strain is obtained from the minimum
249 eigenvalue among all processed wavelength responses.

250 For the specimen F51_D3 tested in shear, an equivalent uniaxial model is formulated as
251 suggested by Plantema (1966) and Kassapoglou (2010): assuming that the principal

compression load occurs at 45° (pure shear), the analytical formulations for wrinkling are used upon “rotating” the relevant quantities in the direction of the applied compression. Here, for skins composed of $\pm 45^\circ$ fabrics, this is equivalent to switching to $0^\circ/90^\circ$ fabrics (see the stacking sequence in Figure 8). It is worth noticing that this approach is expected to be conservative as much as a certain stabilising effect introduced by the tensile load in the direction perpendicular to the compression axis is neglected in the present plane strain setting.

3.2 Radar comparison graph

The results of the considered models are presented in the radar comparison graph of Figure 8 in terms of relative percentage differences between the analytical wrinkling strains and the mean strains at specimen failure (given in Table 2). The dotted line indicates perfect correlation with the tests. A positive percentage shows an optimistic model, a negative percentage shows a conservative model. **The wrinkling strain of analytical models are obtained from the corresponding** load or stress through the equivalent membrane rigidity of the skin. The minimum critical wrinkling strain between symmetric and antisymmetric wrinkling modes is chosen for analysis.

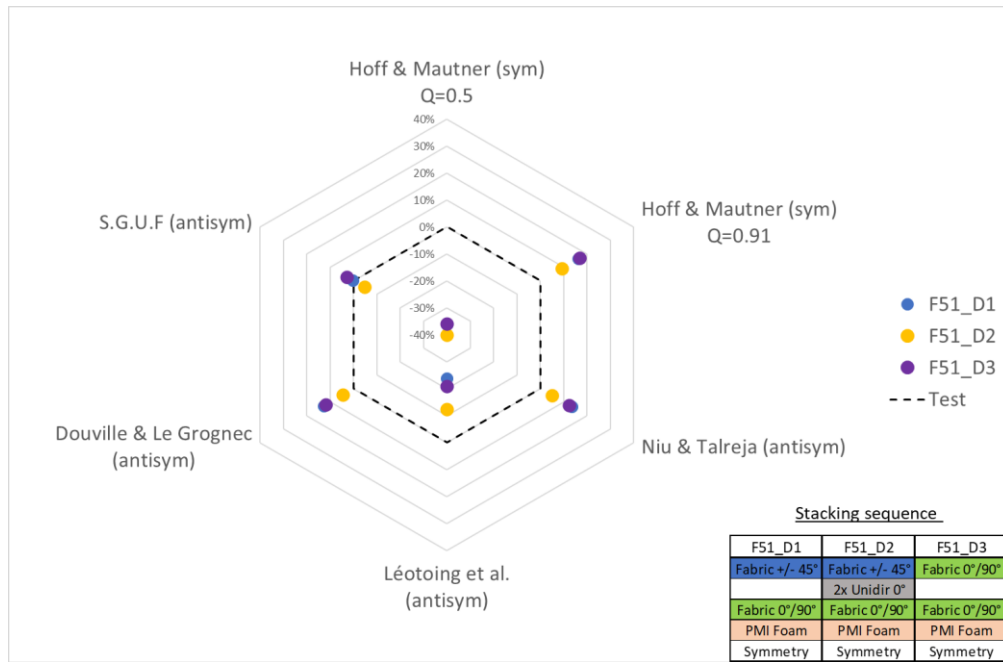


Figure 8: Radar comparison graph between linear models and VERTEX test results.

It is first noticed that the correlation for the specimen F51_D3 is of the same order as for the specimens tested mainly in compression. This confirms that the approach of taking only the compression component seems consistent, even if the specimen is not purely loaded in shear (principal compressive direction at 38°, see § 2.4).

The results show that the models of Douville and Le Grogne, Niu and Talreja and Hoff and Mautner (with $Q = 0.91$) are optimistic while those of Hoff and Mautner's with the knock-down factor $Q = 0.5$ and of Léotoing et al. provide conservative predictions. The quasi-3D analytical S.G.U.F model performs remarkably well for all configurations, yielding at most errors of about 5% on the conservative side. There are many reasons for the analytical expressions to deviate from the experimental measurements. In general, the models from the literature studied here rely on various *ad-hoc* assumptions that can produce a certain inaccuracy depending on the considered problem.

282 The core model **is attributed a major** role in the discrepancy between the computed and
283 experimental buckling loads. All analytical models (including the S.G.U.F model) adopt a
284 constant linear elastic behaviour; **in addition, the models by Niu and Talreja and Douville and**
285 **Le Grogneq rely on the assumption of an isotropic core. In reality, the PMI foam is slightly**
286 **anisotropic (Young's modulus E , tangential modulus G and Poisson's ratio ν are not related**
287 **by Lamé's formula $G = \frac{E}{2(1+\nu)}$) and it** has different properties in tension and compression (see
288 next § 4.4). In the analytical models, however, the modulus has been taken equal to the simple
289 average between tension and compression. Niu and Talreja (1999) have shown that
290 **transverse** shear effects can be important with short wavelengths. Léotoing et al.'s model
291 shows conservative correlations with the tests, **but** the discrepancy with the other models
292 raises questions: **it is worth recalling that** this model **discards the core's axial stiffness** ("anti-
293 plane core") and **postulates** a simplistic distribution of the shear stress **along** the core
294 thickness.

295 Further, questions may be asked about the **definition of an equivalent Young's modulus of**
296 **the** composite laminate skin modelling **that neglects the** membrane/bending coupling terms
297 (matrix B) for specimens F51_D1 and F51_D2,. However, it is worth recalling that the
298 benchmark (Ginot et al., 2021) has shown that, for this type of stacking (similar thickness and
299 stiffness), this coupling is not of major importance in the critical buckling load and should
300 hence not justify such differences in correlations.

301 Finally, the considered analytical bifurcation buckling formulae do not consider any type of
302 initial imperfection, which is known to be a major reason for excessively optimistic failure
303 loads (Ley et al., 1999; Fagerberg and Zenkert, 2005b). Despite the doubtless attractiveness of

such formulae in terms of required computational effort, this drawback questions their applicability for a reliable sizing. So, analytical wrinkling analysis has been enhanced towards initial imperfections in (Kassapoglou et al., 1995; Fagerberg and Zenkert, 2005b). However, its use in pre-design phases may pose difficulties since specific equipment (as DIC) may be required for identifying imperfection amplitudes. Therefore, the classical knock-down factor approach is widely adopted for artificially reducing the theoretical bifurcation loads, as promoted by the early work of Hoff and Mautner. Their **knock-down** coefficient $Q = 0.5$ provides indeed conservative loads in all configurations tested, but it may lead to excessive margins of safety that are detrimental for an optimal lightweight structure.

Imperfection sensitivity is known to play a relevant role in presence of equilibrium paths with an unstable post-buckling response. This is precisely the case of sandwich wrinkling because, as experimentally observed, the weak core undergoes compressive or tensile failure as soon as local skin indentation occurs. Since slight initial dents have been observed by SDIC at the upper skin (see (Ginot et al., 2023) for more details), **the modeling strategy aims to follow the non-linear response including some material and geometrical non-linearities up to failure**. This is the objective of the following sections, in which the experimental-numerical dialogue is extended towards a non-linear FEM accounting for the real initial geometry of the tested panels.

4 Development of a non-linear finite elements panel model

4.1 3D FE panel model definition

The geometry of the sandwich specimen panels, with the integration of the reinforcements (core and skins) around the nominal area (Figure 9) is taken into account in this model. The

monolithic area bolted to the VERTEX test bench is not represented, just a 5 mm wide strip remains: The area modelled by the FEM is thus 400 x 400 mm². ABAQUS S4R elements are used for the skin and monolithic parts and ABAQUS C3D8R elements are used for the core of the sandwich. The skins and the core are assumed to be perfectly bonded and, therefore, they are linked by coincident nodes. Léotoing et al. (2002) recommend a minimum of 4-5 elements per wrinkling half wavelength. The measured wrinkling half wavelengths in the specimens are about 8 mm to 10 mm depending on the sandwich configuration. The horizontal element size is then set to 2 mm in the nominal area. The total number of degrees of freedom is around 720000 for the whole model. The computation is performed using dynamic analysis with ABAQUS Explicit. The choice of this analysis is explained in § 4.4.2.

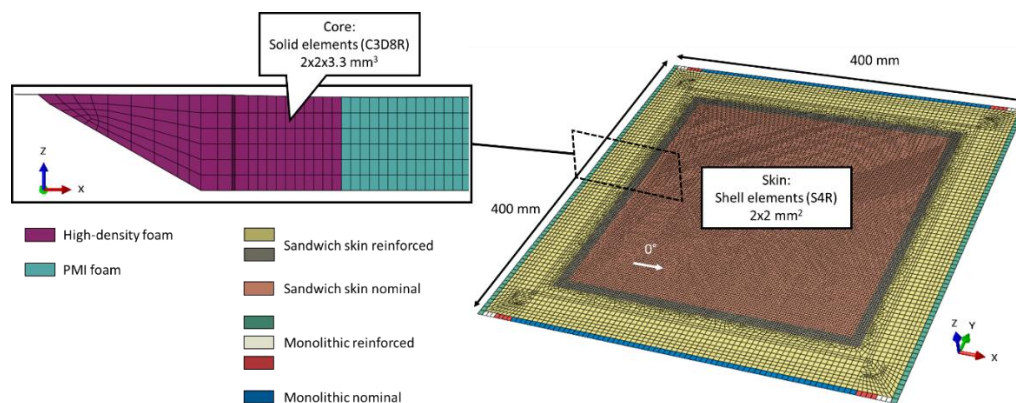


Figure 9: FE panel model definition.

4.2 Boundary conditions imposed by the displacements measured by SDIC

In order to avoid excessively idealized boundary and loading conditions, and in absence of a transfer function explicitly linking the actuator forces of the VERTEX bench to the load acting on the specimen, Stereo Digital Image Correlation (SDIC) data are extracted and used to apply a loading path in the numerical model. This approach has been successfully developed and used for the previous experimental and computation dialogues on VERTEX test campaigns

(Serra et al., 2017a; Trellu et al., 2020). It consists of imposing the displacements (U,V,W) measured by SDIC on a rectangular frame of upper face nodes (red in Figure 10), plus out-of-plane displacements (W) on 3 additional rectangular frames (orange in Figure 10).

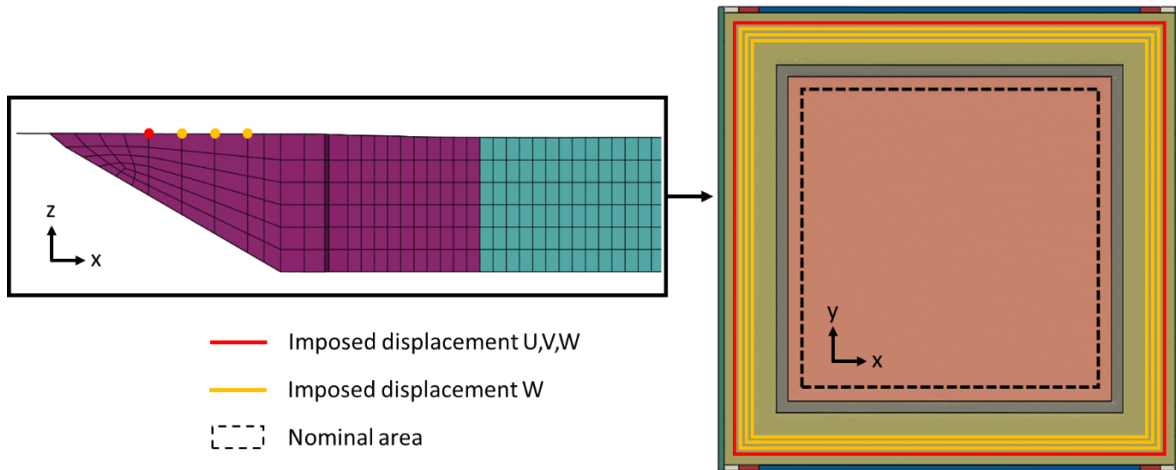


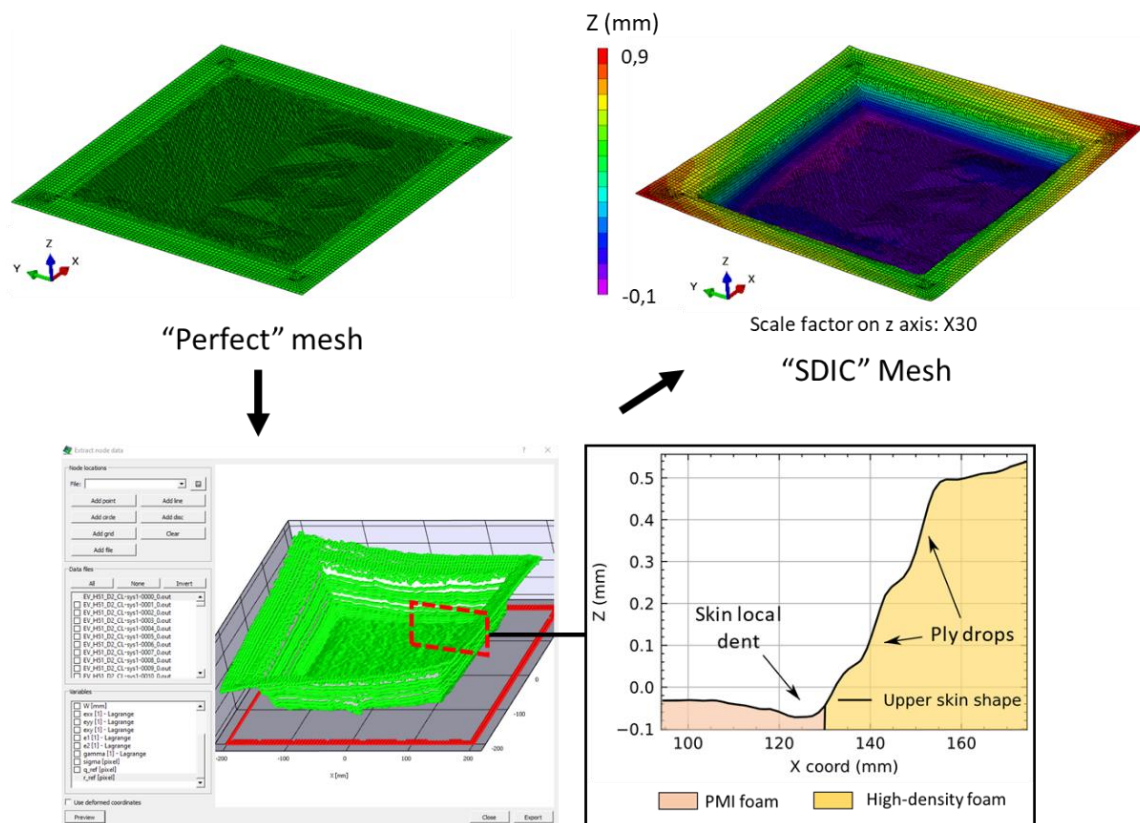
Figure 10: SDIC loading condition imposed in the FEM by four imposed displacement frames. Rotations are then introduced by the out-of-plane displacement gradient between the loading frames (Sztefek and Olsson, 2008). Displacements are implemented in the model as amplitudes against time and are linearly interpolated between two successive SDIC measurements to represent their evolution during the test.

4.3 Initial imperfections

4.3.1 Mesh building based on SDIC data

The introduction of measured imperfections from a real part in a finite element analysis has been strongly studied in the Thin-Walled Structures community. The most commonly used method to approximate geometrical imperfections is using a double Fourier series (Arbocz, 1982). In addition, this formulation allows the Fourier coefficients to be random variables for probabilistic analysis (Wagner et al., 2020). Recently, the use of double Fourier for mesh generation based on SDIC data was performed to model the effects of geometric

imperfections on the buckling behaviour of woven composite cylindrical shell structures (Xin et al., 2022). In our case, generating imperfections through a double Fourier series is not used. Fourier series such as a sum of periodic sine function would not **correctly** represent the ply drops offset, present in the sandwich skins between nominal and reinforced **areas**, because ply drops are not periodic. Another method is to use SDIC measurements of the initial specimen profile and apply them directly to generate a mesh. This method has already been used on CFRP panels under compression (Featherston et al., 2012). A perfect mesh is first made. Then, the out-of-plane positions, z , are extracted from SDIC data at the corresponding x and y positions of the upper skin nodes of the perfect mesh (Figure 11). In nodes at the FEM boundaries, where SDIC data are not consistent or available (SDIC measuring window edges), linear extrapolation from the nearest measured data points is used. The “SDIC” mesh has shown that very small ripples can trigger wrinkling localisation. It is necessary to dissociate the ripples due to the measurement uncertainty from the actual imperfections. The parameters used for the SDIC are recommended by the DIC software to minimise data noises from the image characteristics (resolution, contrast, etc.); Subset size is 35 px; step size is 15 px; with a pixel size equal to 0.2 mm. With these parameters, the average confidence margin of the measurements is about 0.01 pixel, which is equal to 0.002 mm. The imperfections present in the specimens were measured at about 0.04 mm in out-of-plane direction z , which is an order of magnitude greater than the SDIC confidence margin.



Out-of-plane coordinate z extraction from SDIC data at zero load

Figure 11: Upper sandwich face mesh construction from measured SDIC out of plane coordinates z.

Note that the measured surface is the upper face of the skin, the ply drop offsets are integrated into the "SDIC" mesh. The thickness offset in the shell elements of the upper skin is then set to "top" (Figure 12).

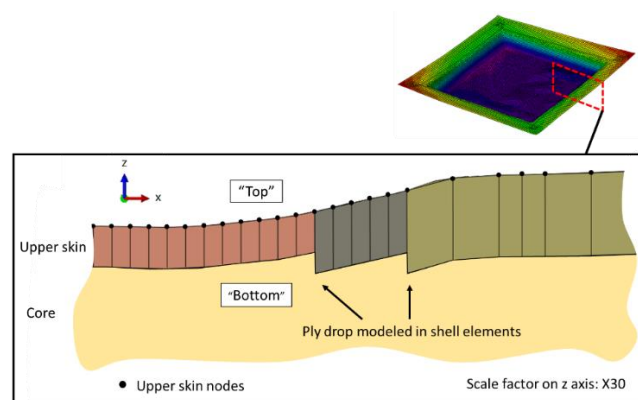


Figure 12: Thickness offset modelled in the shell elements of the upper surface in the "SDIC" mesh.

4.3.2 Effects of defects

Figure 13 illustrates the influence of the initial imperfections introduced into the mesh on in-plane and out-of-plane strain. By comparing the results from a perfect mesh (left image in Figure 13 (a)) and those from the “SDIC” mesh with imperfections (right image in Figure 13 (a)), we observe:

(1) In Figure 13 (a), wrinkling waves are represented by blue areas with high strain gradients induced by the local bending of the wrinkling waves. In the perfect mesh, the wrinkling pattern is smooth and straight, whereas in the “SDIC” mesh it is less regular and follows the localisation and the geometry of the initial imperfections. **The dissymmetry of the wrinkling zone displayed in the “perfect mesh” results is induced by the loading which is a pure compressive loading along X axis (Table 2). This dissymmetry appears slightly less pronounced in the “SDIC mesh” results. This difference is likely to be due to the non-constant top surface level (z-position due to the geometric imperfections)**

(2) Figure 13 (b) is the plot of strain evolution of the top and bottom faces in the upper skin of the sandwich at the inspection point (red point in Figure 13 (a)). The Initial imperfections in the “SDIC” mesh induce local bending effects. This is shown by the difference in the in-plane strain evolution between the top and bottom faces (solid lines in Figure 13 (b)). The evolution rapidly becomes non-linear and the buckling onset is characterised by a progressive growth of the non-linearity. In contrast, in the perfect mesh (dotted line in Figure 13 (b)), the strain difference between the top and bottom faces is almost zero and linear until the bifurcation (computation progress equals 1). These local bending effects generate high out-of-plane strains in the core (Figure 13 (c)) from the beginning of the loading. **Due to the low mechanical performances of the PMI foam, the out-of-plane** strength can be reached rapidly and trigger

the core to fail. Consequently, a more accurate modelling of the core is proposed in the next subsection.

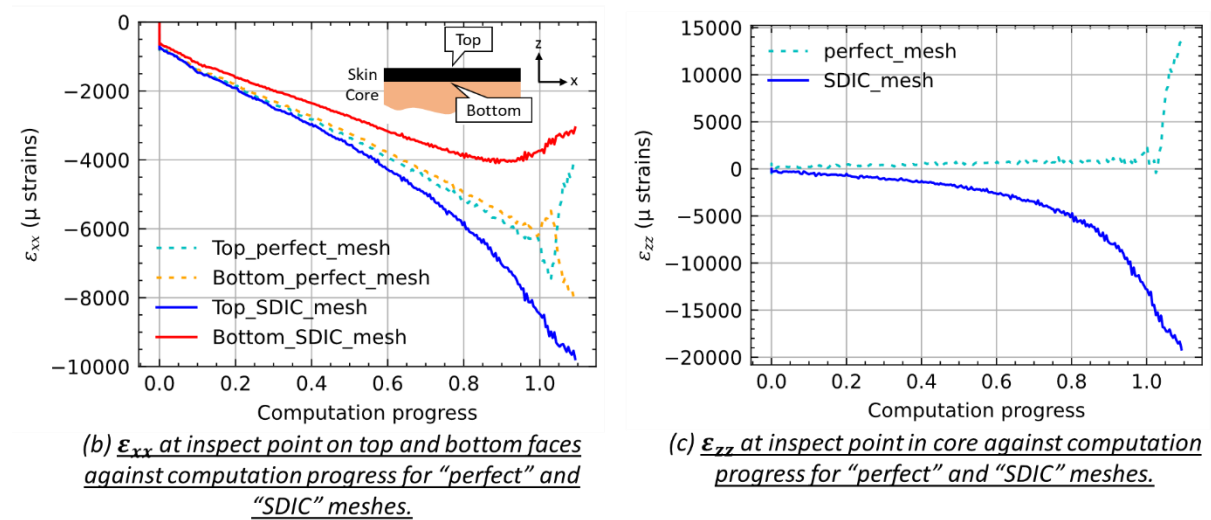
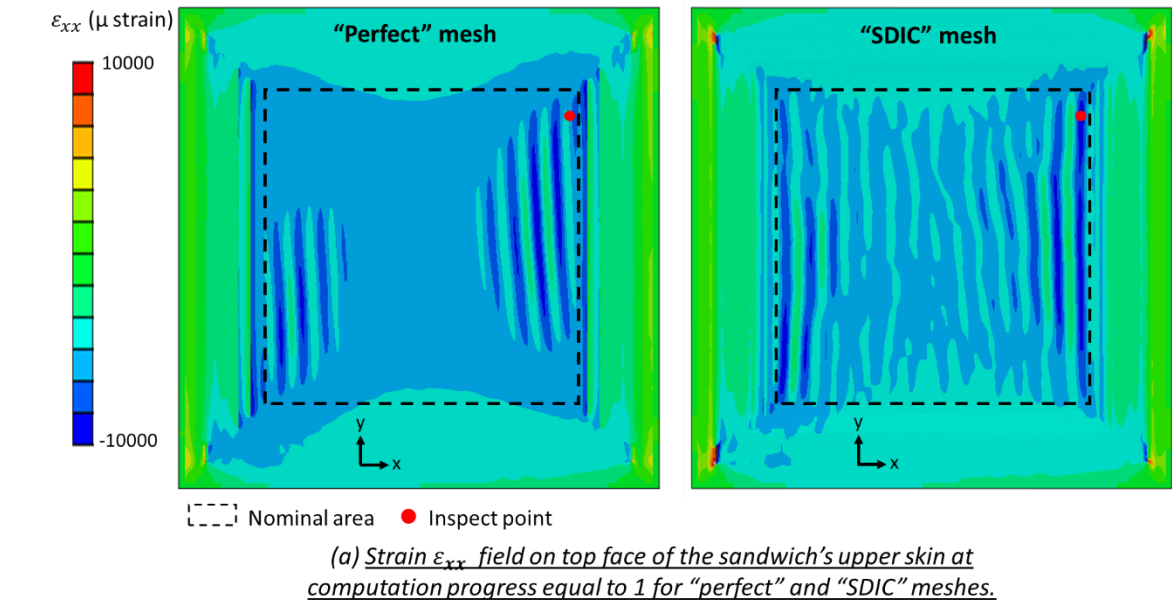


Figure 13: FE results of "Perfect" and "SDIC" meshes from the loading condition of specimen F51_D1 (axial compression)."

4.4 Core behaviour modeling

4.4.1 Constitutive law for the core

PMI foam exhibits different mechanical behaviours in compression and tension. In compression, the foam behaves like a ductile material where an elastic response is first

observed, followed by a plateau corresponding to the buckling of the cell walls and then the cell walls interact, increasing the overall stiffness of the foam (called densification). In tension, the behaviour is rather fragile, with brittle failure. In our case, the difference in mechanical characteristics between compression and tension is significant, with the tension modulus and strength being more than twice the compression ones. **Abrate (2008) shows that hydrostatic pressure has an important effect on foam failure. Since the anisotropy in the elastic regime is not very important (Wang et al., 2010), an isotropic bi-modulus constitutive law is assumed and implemented in the principal directions. In compression, a perfect elastoplastic model is used. The foam densification is not modelled here, because it appears for very large strains not reached in our experiments. In tension, an elastic response is used with damage modelled by element deletion (Figure 14). Note that a yield surface with a crushable foam model is available in ABAQUS software, but it does not provide the possibility of working with bi-modulus behaviour. In compression, experimental results indicate that the compressive strength is limited by the buckling of the cell walls and show that it can be closely approximated by a maximum principal stress criterion (Gibson and Ashby, 1997). So, a maximum principal stress criterion is chosen as the yield surface in compression and tension (Figure 14). This greatly simplifies the integration of plastic strains $\dot{\varepsilon}^p$ which are classically taken normal to the yield surface. An elliptical yield surface such as described by Deshpande and Fleck (2000) or Huo et al. (2022) would introduce a more complex calculation.**

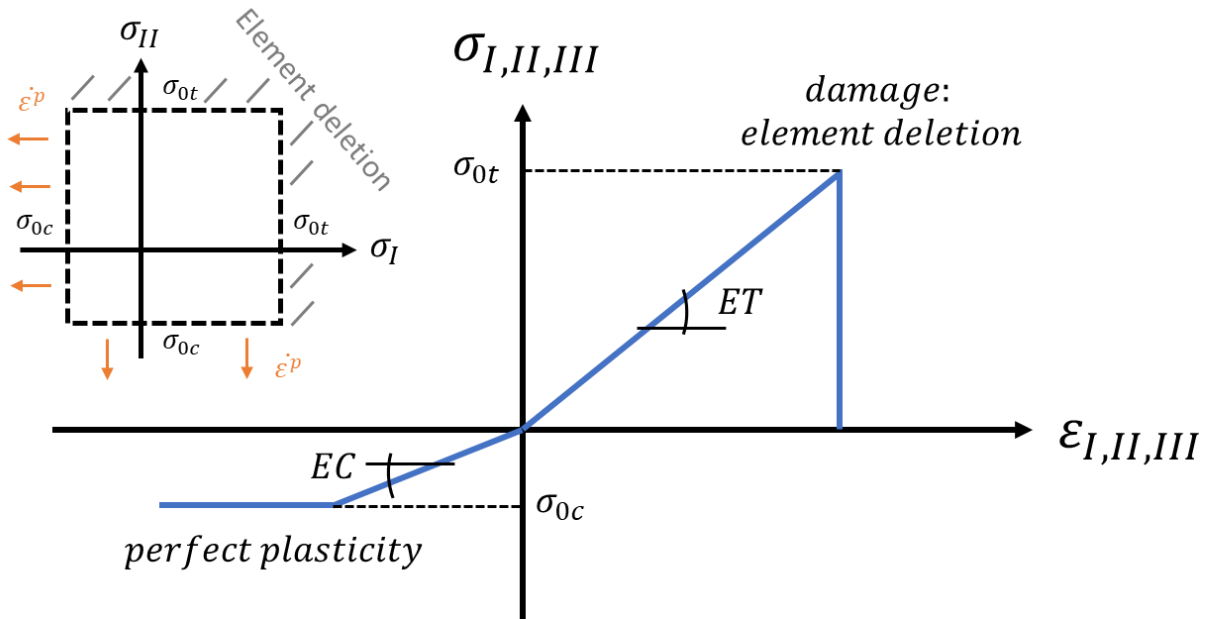


Figure 14: Constitutive law and yield surface of the PMI foam core used in the FE panel model. Parameters ET ; EC ; σ_{0c} ; σ_{0t} are calibrated from characterisation test campaigns in traction (ASTM C297 (ASTM C297, 2004)) and compression (ASTM C365 (ASTM C365, 2011)).

4.4.2 Explicit computation

The constitutive law of the foam was first implemented with implicit computations using ABAQUS UMAT. However, **the resulting elasto-plastic instability problem** led to difficult convergence problems, a difficulty also noticed by Leotoing (2001). The post-buckling behaviour was not reached in implicit computation. The choice of dynamic explicit computation was therefore made, and the constitutive law was implemented with ABAQUS VUMAT. The explicit solver can be relevant for quasi-static computations when these are subject to convergence problems (significant non-linearity, complex contact management). In the case of buckling, the explicit analysis allows the highly nonlinear post-buckling structural response to be followed (Bisagni, 2000). The use of an explicit solver for the solution of a quasi-static problem has some particularities that have to be dealt with (Pinho, 2005; Serra et al., 2016). Relatively to a standard implicit solver, an explicit solver needs very small increments (depending on the size of the element). Thus, analysis usually requires a large number of

increments, and a considerable numerical displacement speed compared to the actual quasi-static problem. Kinetic energy is then introduced, and a damping system is needed to reduce the dynamic vibration. During these steps, a numerical error can accumulate, and the work of external forces can be converted into energy other than the internal energy, such as kinetic energy, hourglass control energy and damping energy. It must be checked that additional energy is kept at a negligible level by selecting the right numerical displacement speed while keeping a reasonable calculation time. The numerical displacement speed taken is 100 mm/s with a time increment of 10^{-7} s. On the other hand, increasing the stable time increment prevents unwanted vibrating effects. The ABAQUS function "*MASS SCALING" (Abaqus Analysis user's Manual) was used to artificially increase the mass of the model. To ensure that changes in the mass and consequent increases in the inertial forces did not alter the solution significantly, a calculation was performed with a numerical displacement speed that was a quarter of the initial one and showed similar results.

In the test process, residual strains are induced in the specimen when it is bolted onto the VERTEX test bench (see detail in (Ginot et al., 2023)). This is transcribed in the FEM's loading conditions with a preload imposed by large displacements in the four displacement frames (Figure 10). It is necessary to dissipate the kinematic energy introduced by the preload as far as possible. The displacements are too large to be handled by the numerical displacement speed without a significant increase in computation time. The solution shown, in Figure 15, is the simulation of three steps of relaxation after the preload step. In these steps, the velocity of each node of the FEM is set to zero to keep the kinematic energy at zero, then left free so that the panel can take its distorted equilibrium form. During these relaxation steps, the imposed displacements are kept constant (the red dotted line in Figure 15 is the average

displacement X of the left side of the first displacement frame in Figure 10). The test loading conditions are then introduced. This solution has already been used to dissipate energy after impact in (Serra et al., 2021).

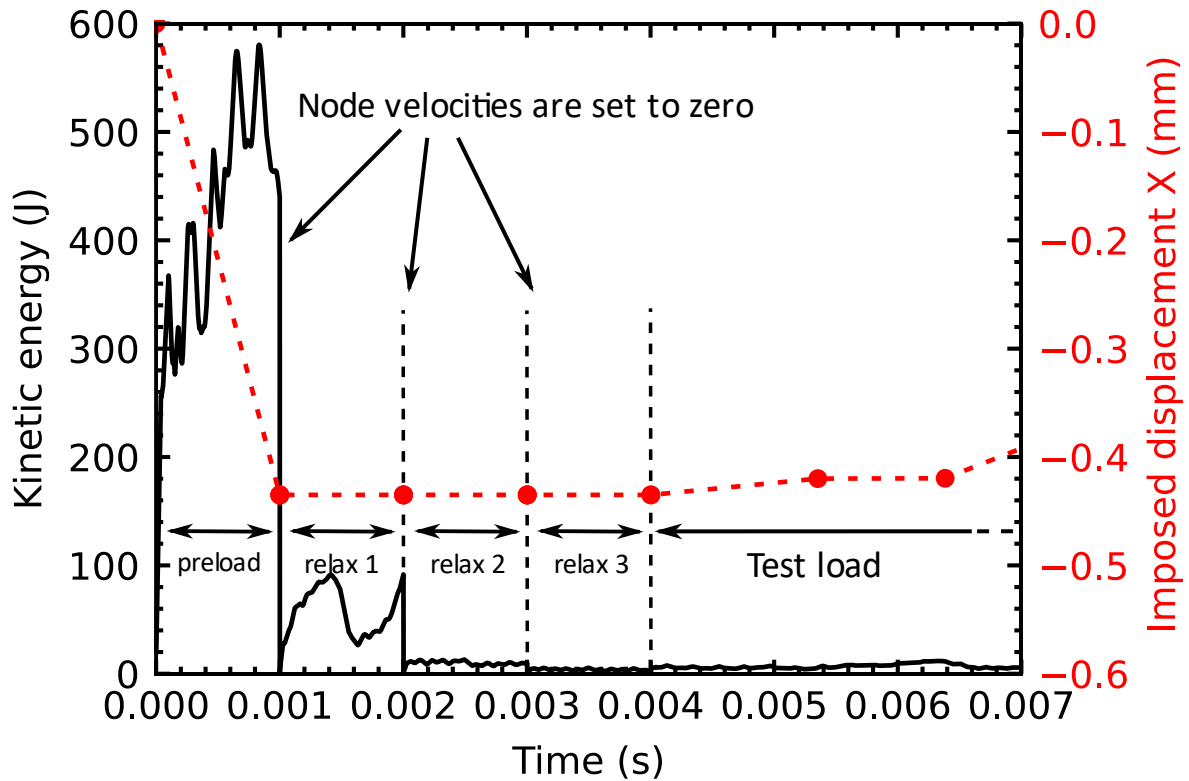
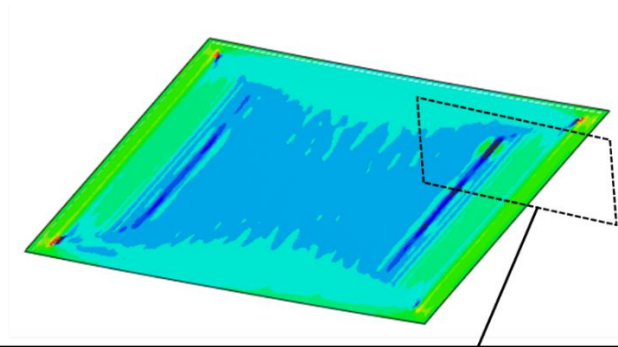


Figure 15: Overall kinematic energy versus time in FEM from the loading condition of specimen F51_D1. 3 relaxation steps allow kinetic energy dissipation from large displacements in preload step.

4.4.3 Effects of the compressive elastoplastic and tensile damage core behaviour

The study of the core non-linear behaviour in the local instability is not completely original. In the literature, several authors have tried to add this parameter to their numerical models but have remained at the beam scale. Stiftinger and Rammerstorfer (1997) included a core crushing behaviour in a sandwich beam FEM and reported a slight decrease of the maximum load and a sudden drop in the load. Léotoing et al. (2002) used a perfect **elastoplastic** model with a von Mises yield function, where the constitutive law is calibrated from a uniaxial

495 compression test. They noted that the plastic strains are located where wrinkling occurs. The
496 transition from the elastic to the plastic state was immediately followed by a drastic decrease
497 in the overall stiffness of the sandwich beam **In our built-up structure, inclusion of the**
498 **compressive elastoplastic and tensile damage behavior of the core allows to reproduce the**
499 **observed failure scenario.** Firstly, plastic strains develop locally at the skin interface, then,
500 large out-of-plane strains make the core fail in tension (Figure 16).



Computation process	Local cross section	
	PMI foam	High-density foam
90%		
95%		
98%		
99.5%		
100% Tensile failure (elements deleted)		


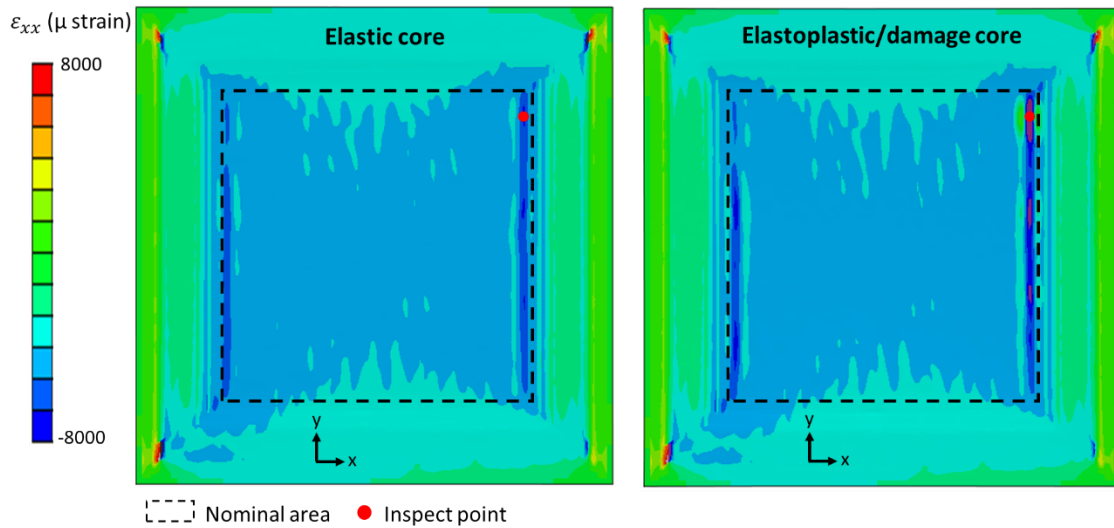
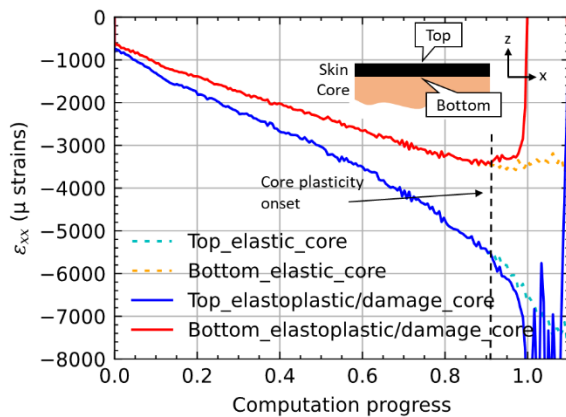
 Plastic strains in solid elements

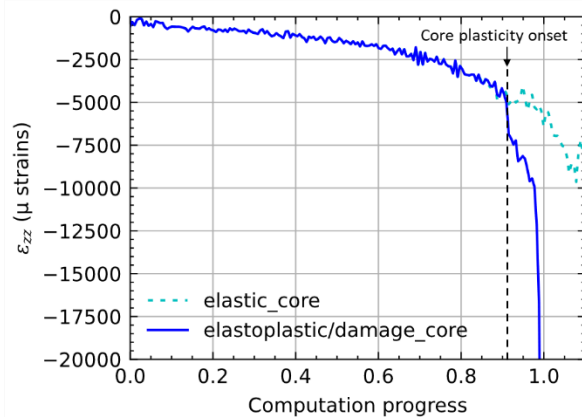
Figure 16: FEM cross sections with elastoplastic+damage constitutive law for the core. Plastic strains develop locally, then the core fails in tension (modelled by element deletion).



(a) Strain ϵ_{xx} field on upper skin of top face of the sandwich at computation progress equal to 1 for elastic and elastoplastic+damage core modeling.



(b) ϵ_{xx} at inspect point on top and bottom faces against computation progress for elastic and elastoplastic+damage core modeling.



(c) ϵ_{zz} at inspect point in core against computation progress for elastic and elastoplastic+damage core modeling.

Figure 17: FE results of elastic and elastoplastic+damage core modelling from loading condition of specimen F51_D1 (compression). The constitutive law introduces an elastoplastic behaviour in compression and an elastic response with damage modelled by element deletion in tension (see Figure 14).

Figure 17 illustrates the results of a comparison between a bi-modulus full elastic core behaviour (left image in Figure 17 (a)) and one with the elastoplastic and damage behaviour of the core added (right image in Figure 17 (a)). The transition from an elastic to a plastic state tends to develop non-linear, in-plane strains (solid line in Figure 17 (b)) and out-of-plane strains (solid line in Figure 17 (c)), which increase rapidly with loads. The plastic state develops locally in the panel under the wrinkling waves with maximum amplitude, magnifying the non-

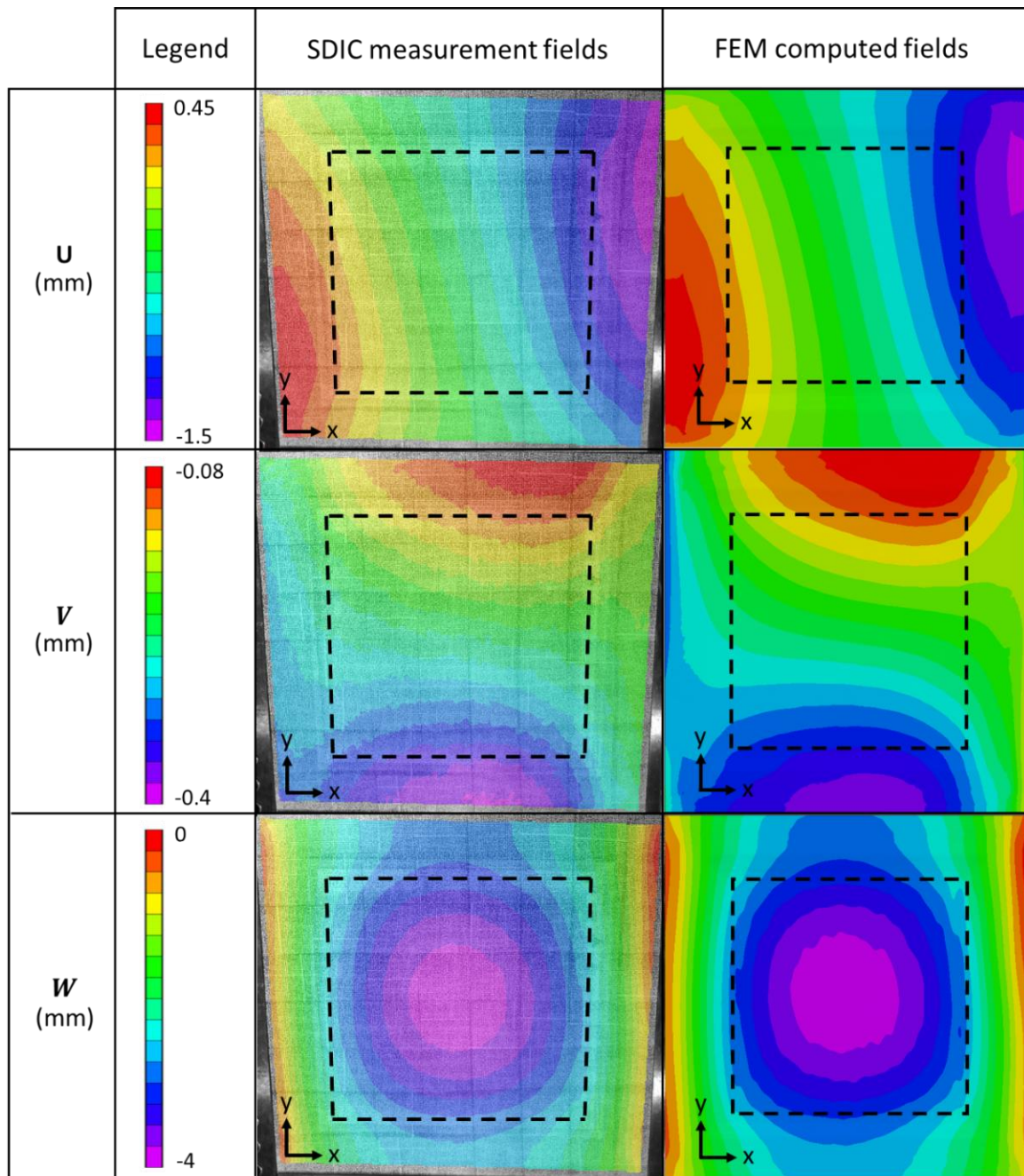
linearity and localising the wrinkling failure (purple area in Figure 17 (a) right image). **The jump observed in (Figure 17 (b) and (c)) at the onset of plasticity is due to the implemented perfectly elastoplastic behaviour.** The integration of the elastoplastic and damage behaviour of the core makes the panel fail brusquely (considering when the first tensile failure of the core occurs with the computation progress equal to 1), whereas, in the case of purely elastic core behaviour, buckling is progressive and buckling onset is not easy to interpret.

5 Non-linear finite element model of panel: Experimental and computation dialogue

5.1 Specimens under compression

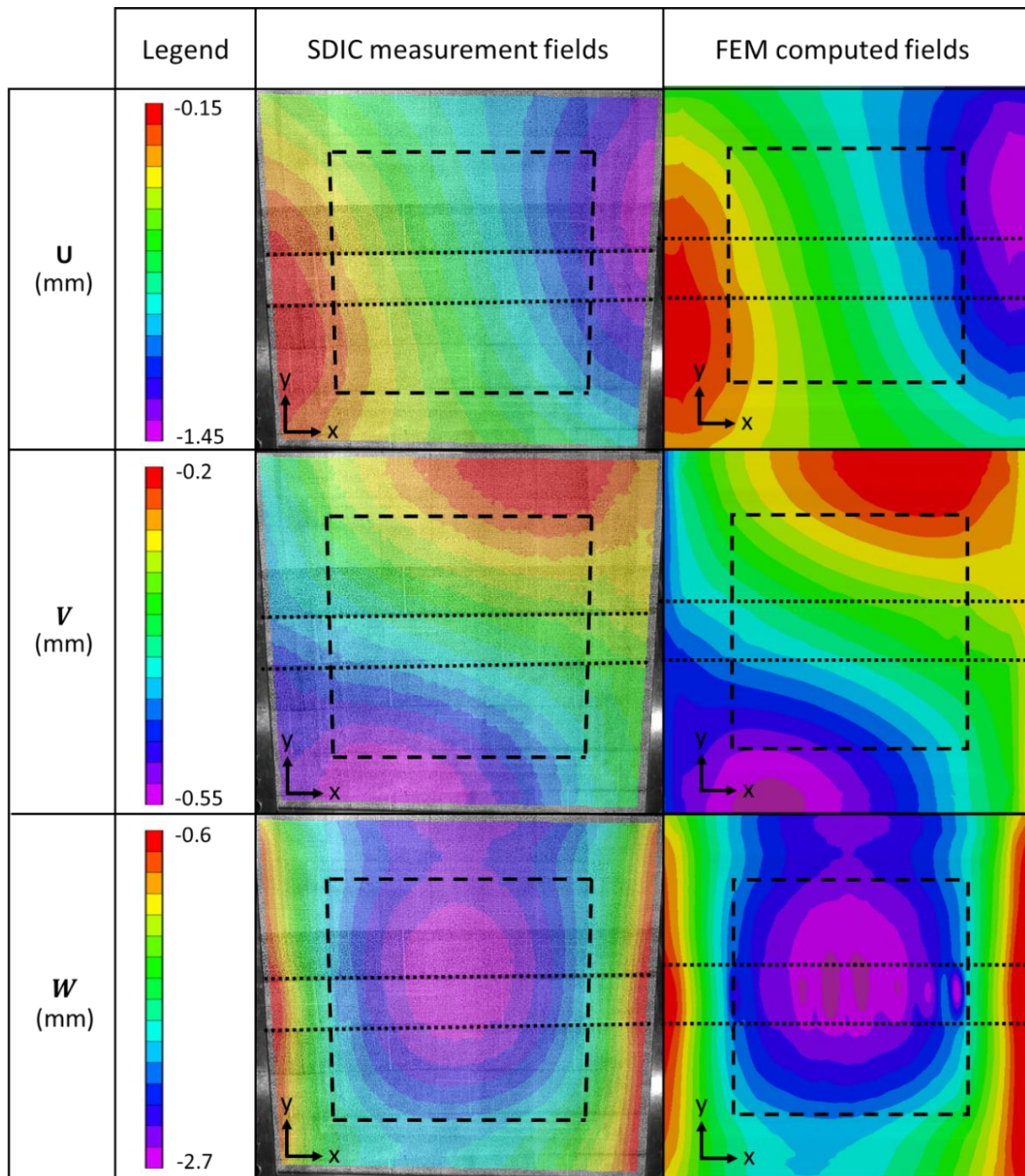
5.1.1 Overall behaviour

Figure 18 and Figure 19 show the displacement fields in the upper face for specimens F51_D1 and F51_D2 obtained by SDIC versus those computed by the FEM. Good agreement is found between experimental and numerical displacement fields. **In-plane** and out-of-plane displacement fields computed by FEM are similar to those measured in the nominal area. This confirms that the loading condition methodology developed in § 4.2 is effective to introduce the loading path imposed by the VERTEX test bench in the sandwich specimen.



Nominal area

Figure 18: Displacement fields: comparison between experimental measurements and FEM results of the upper face of specimen F51_D1 under compressive loading. Frames were taken just before the core failed in tension in the FEM (93% of test progress).

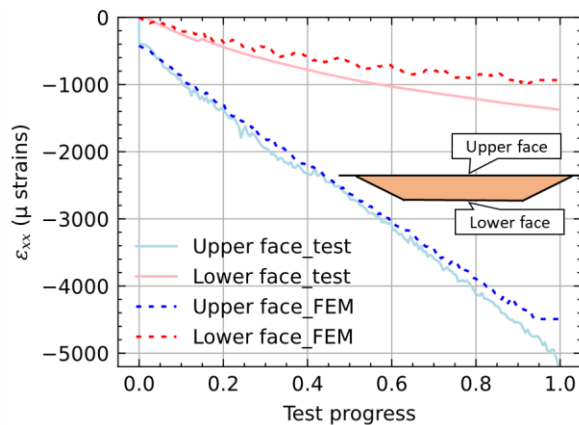


Nominal area
 Unidir 0° ply area

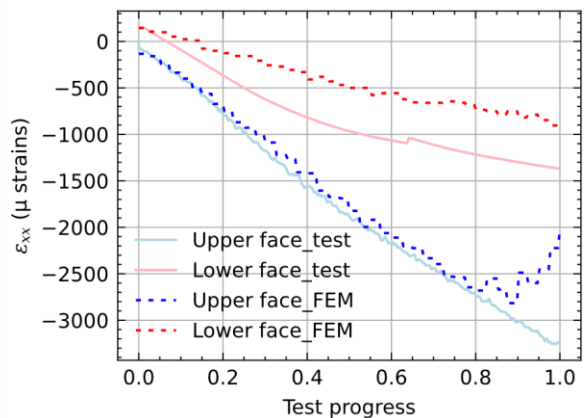
Figure 19: Comparison of displacement fields between experimental measurements and FEM results of the upper face of specimen F51_D2 under compressive loading. Frames were taken just before test failure (99% of test progress).

The specimen panels bend globally, as a consequence of the asymmetric geometry (see § 2.1, Figure 3 and (Castanié et al., 2002)), and the upper skin is more loaded than the lower skin (Figure 20). The FEM represents the global membrane and bending stiffness of the sandwich

panels adequately, as shown by the acceptable correlation in the strain of the upper and the lower skins in the centre of the panel (Figure 20). This confirms the relevance of the mechanical and geometrical characteristics used for the simulation. **However, the numerical models are slightly less stiff in bending than either of the specimens, as can be also inferred from the higher values of out-of-plane displacements W in Figure 18 and Figure 19. As a result, the computed compressive strains in the bottom skin are smaller due to the higher tensile load induced by the larger global bending of the panel (Figure 20). As already pointed out by Castanié et al. (2002), the bottom skin of the VERTEX panels is very sensitive to load introduction and local ply drops in the transition region, which can explain the discrepancy. Note that the strains introduced by the assembly of the sandwich panel on the test bench can be seen in Figure 20 and is correctly taken into account in the FEM.**



(a) Strain ϵ_{xx} in the upper and the lower faces centre against test progress for the specimen F51_D1.



(b) Strain ϵ_{xx} in the upper and the lower faces centre against test progress for the specimen F51_D2.

Figure 20: Strain ϵ_{xx} in the upper and the lower skins against test progress for specimens F51_D1 and F51_D2.

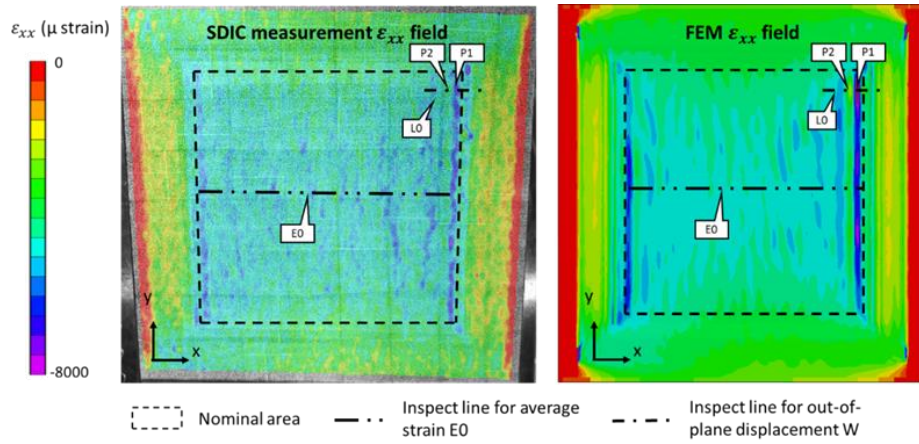
5.1.2 Local behaviour

In Figure 21 (a) and Figure 22 (a) local gradients in ϵ_{xx} strain fields, represented by deep blue areas in SDIC measurements as well as in the simulation results, are present at the edge of the nominal area.

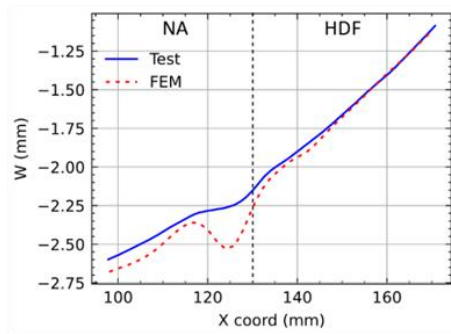
This reflects a local bending induced by wrinkles. Wrinkles are shown with the profiles of the curves in Figure 21 (b) and Figure 22 (b) for out-of-plane displacement and in Figure 21 (c) and Figure 22 (c) for strain ϵ_{xx} on inspect line L0 (see Figure 21 (a) and Figure 22 (a)). In Figure 21 (d) and Figure 22 (d), the strain evolutions **at inspect points** P1 and P2 are firstly linear with respect to the load and then become non-linear. This is a consequence of the bending effect of the wrinkling wave, which appears at around 80% of the failure load. The strain slopes at P1 and P2 (see Figure 21 (d) and Figure 22 (d)) differ from the averaged one E0. This is due to geometric imperfection generating out-of-plane displacements, which affect local in-plane strains. The difference in slopes and non-linearity at the end of the test, which reflects the onset of buckling, are well represented in the simulations for both specimens. For the specimen F51_D1, the location of the wrinkling predicted by the simulation is consistent with that experimentally observed by SDIC. The profiles of the curves of Figure 21 (b) and (c) show a good match between the test (solid blue lines) and the FEM (dashed red lines), even though larger gradients are present in FEM results. Larger gradients show that the simulation is conservative. Wrinkling is quickly followed by tensile failure of the core, which occurs at 93% of test progress (Figure 21 (b)). At the time studied, i.e. at 93% of the test progress, the local non-linearity resulting from the buckling process is well underway in the simulation whereas, in the test, buckling is just starting to occur. The conservatism of the simulation can be explained by the methodology for introducing imperfections. SDIC measurements of the initial

580 profile's upper face are directly applied to generate the mesh, which implies that the
581 measured curvature is constant over the thickness of the skin. For example, a variation in skin
582 thickness will be simulated as a ripple of the whole skin. It is likely that this method introduces
583 imperfections of greater magnitude than the real ones.

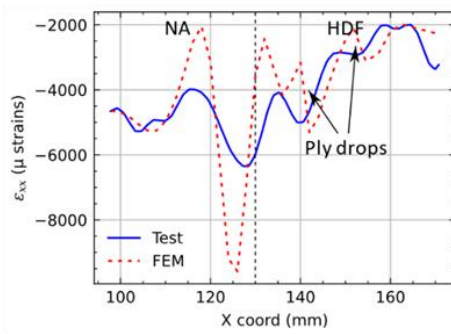
584



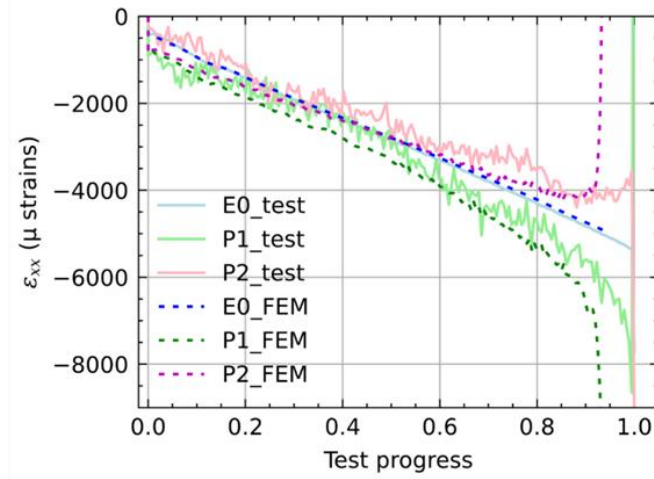
(a) Inspect points and lines on strain ϵ_{xx} field at 93% of test progress.



(b) Out-of-plane displacement on inspect line LO at 93% of test progress. NA=Nominal Area; HDF=High-Density Foam

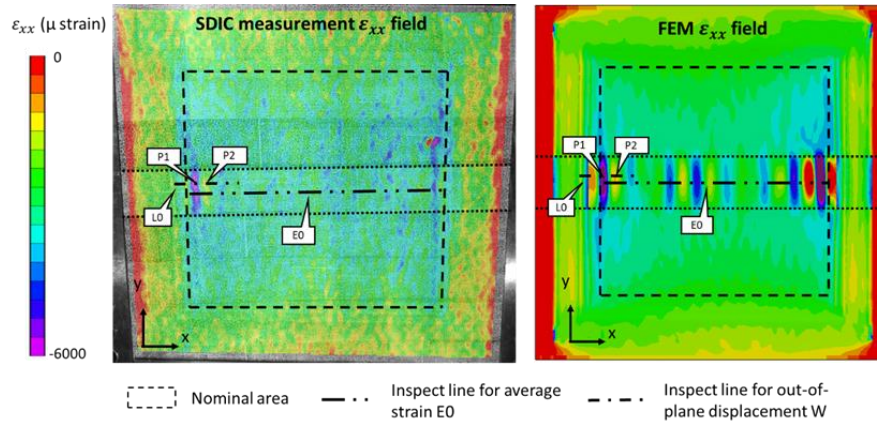


(c) ϵ_{xx} on inspect line LO at 93% of test progress. NA=Nominal Area; HDF=High-Density Foam

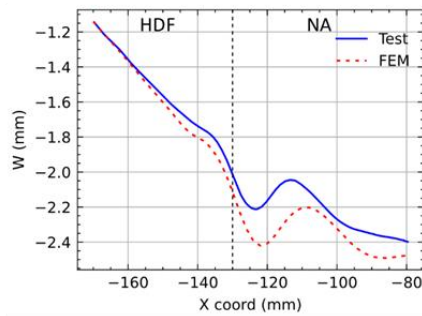


(d) Strain ϵ_{xx} of inspect points P1 and P2 and average strain E0 against test progress.

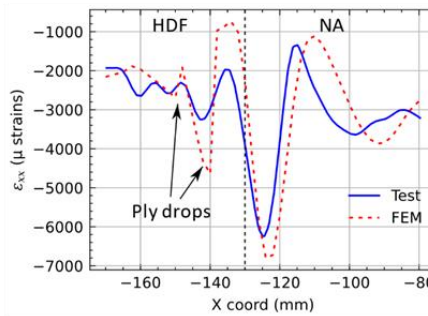
Figure 21: Comparison of fields and curves between test and FEM for specimen F51_D1.



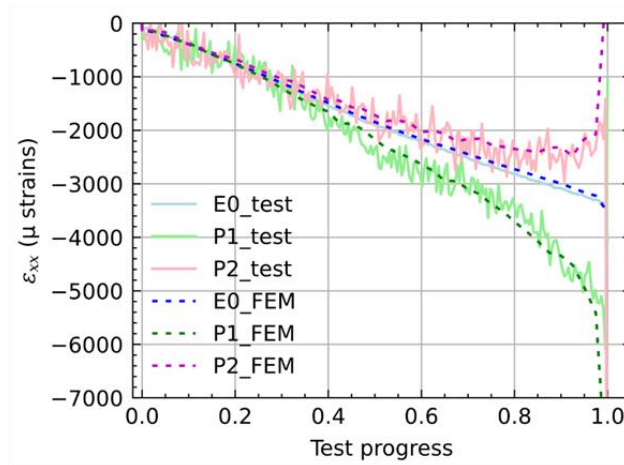
(a) Inspect points and lines on ϵ_{xx} field just before failure.



(b) Out-of-plane displacement on inspect line LO just before failure. NA=Nominal Area; HDF=High-Density Foam



(c) ϵ_{xx} on inspect line LO just before failure. NA=Nominal Area; HDF=High-Density Foam



(d) ϵ_{xx} of inspect points P1 and P2 and average strain $E0$ against test progress.

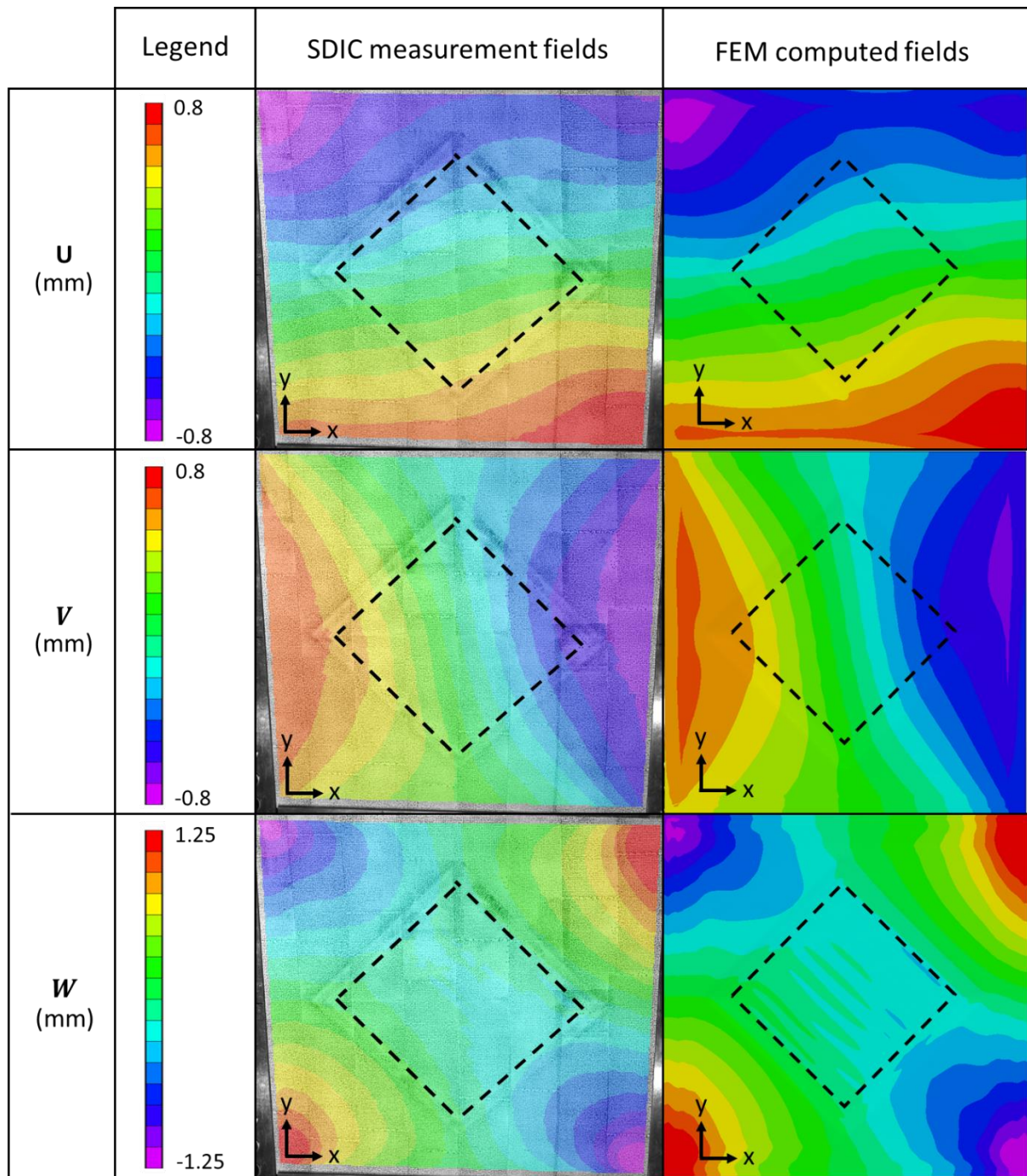
Figure 22: Comparison of fields and curves between test and FEM for the specimen F51_D2.

For specimen F51_D2, note that a 60 mm wide strip of two Unidir 0° plies is added in the centre of the panel (Figure 22 (a)) and the wrinkling is positioned in this stiffened area, which drains the loads. Several wrinkles appear in the simulation, whereas only one is present in the test (Figure 22 (a)). This might be explained by the fact that the initial geometrical imperfections are less marked here than for specimen F51_D1 (this has already been suggested in section 3) and are not sufficient to localise the buckling to a particular area in the simulation. Nevertheless, a wrinkle is present where wrinkling is observed in the test. The profiles of the curves in Figure 22 (b) and (c) show a very good match between the test (solid blue lines) and the FEM (dashed red lines).

5.2 The specimen under shear (F51_D3)

5.2.1 Overall behaviour

Figure 23 shows the displacement fields measured by SDIC in the upper face of specimen F51_D3 tested under shear loading and enables them to be compared with those computed by the FEM. The comparison is made just before the test failure. Here again, the correlation between experimental and numerical displacement fields is good.



Nominal area

609

610 *Figure 23: Comparison of displacement fields between experimental measurements and FEM*
611 *results for the upper face of specimen F51_D3 under shear loading. Frames were taken just*
612 *before test failure (99% of test progress).*

The correlation of the shear strain in the upper and the lower faces in the centre of the panel is acceptable (Figure 24). The FEM represents the global shear stiffness of the sandwich panel adequately.

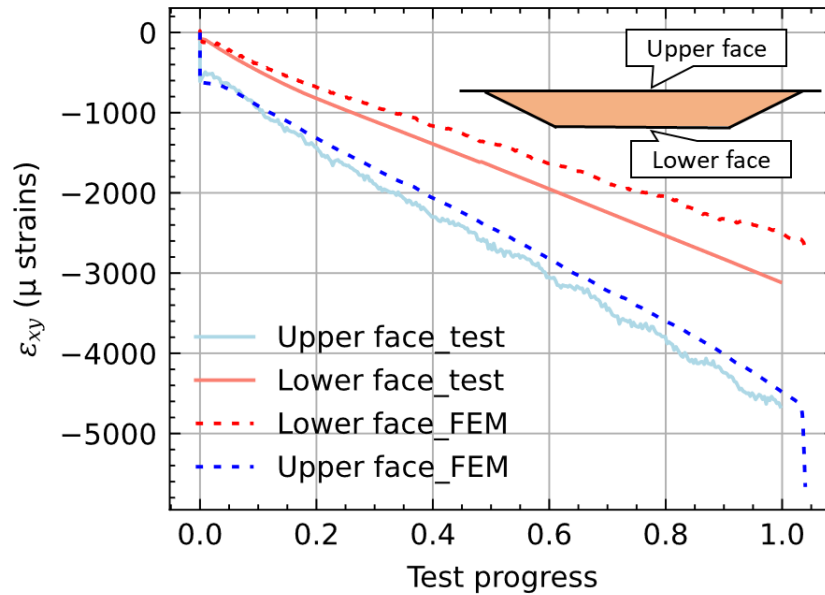
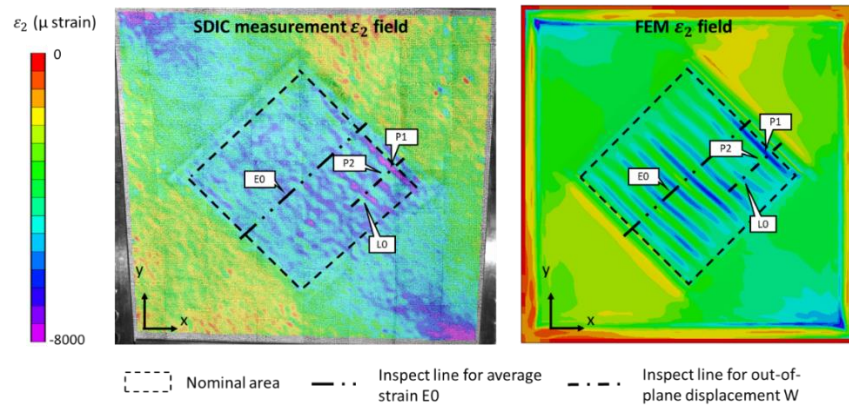


Figure 24: Shear strain ε_{xy} of the centre of the upper and the lower faces against test progress.

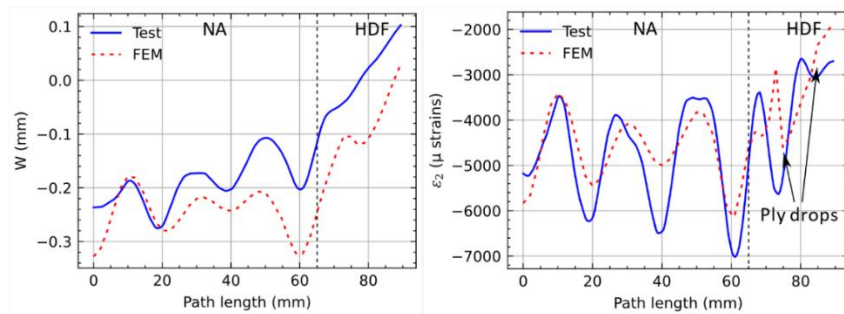
5.2.2 Local behaviour

Several wrinkles were observed in the nominal area. They are shown in Figure 25 (a) by the local gradients in principal compressive ε_2 strain fields and, in Figure 25 (b) and (c), by out-of-plane displacement and ε_2 strain curve profiles in the wrinkling area. Note that the principal compressive direction is about 38° from the x-axis, which is why the principal compressive strain ε_2 is expressed instead of the 45° strain, which would be pertinent in pure shear loading. The simulation is consistent with the localisation of the wrinkles. The observation of several wrinkling waves allows an accurate determination of the half-wavelength of the buckling pattern; it is around 10 mm. The simulation is doubly validated by the very good correlation between (1) the average strain state and (2) the length of the half-wavelength of the buckling

629 pattern. As in the compressive tests, the evolution of the principal compressive strains ϵ_2 at
630 inspect points P1 and P2 shows a linear trend versus loading, followed by a non-linear regime
631 at the end (Figure 25 (d)). Again, this can be attributed to the onset of local buckling that
632 occurred at around 80% of the failure load. The simulation follows the wrinkling phenomenon
633 very well, while being slightly optimistic (Figure 25 (d)).

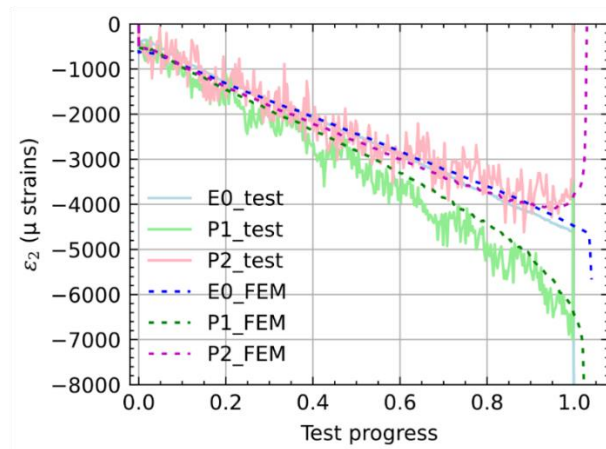


(a) Inspect points and lines on principal compressive strain ϵ_2 field just before failure.



(b) Out-of-plane displacement on inspect line L0 just before failure. NA=Nominal Area; HDF=High-Density Foam

(d) ϵ_2 on inspect line L0 just before failure. NA=Nominal Area; HDF=High-Density Foam



(e) principal compressive strain ϵ_2 of inspect points P1 and P2 and average strain E0 against test progress.

Figure 25: Fields and curves comparison between test and FEM for the specimen F51_D3.

5.3 Radar comparison graph

In this section, the radar comparison graph shown in § 3.2 is reused with the results from the non-linear FEM.

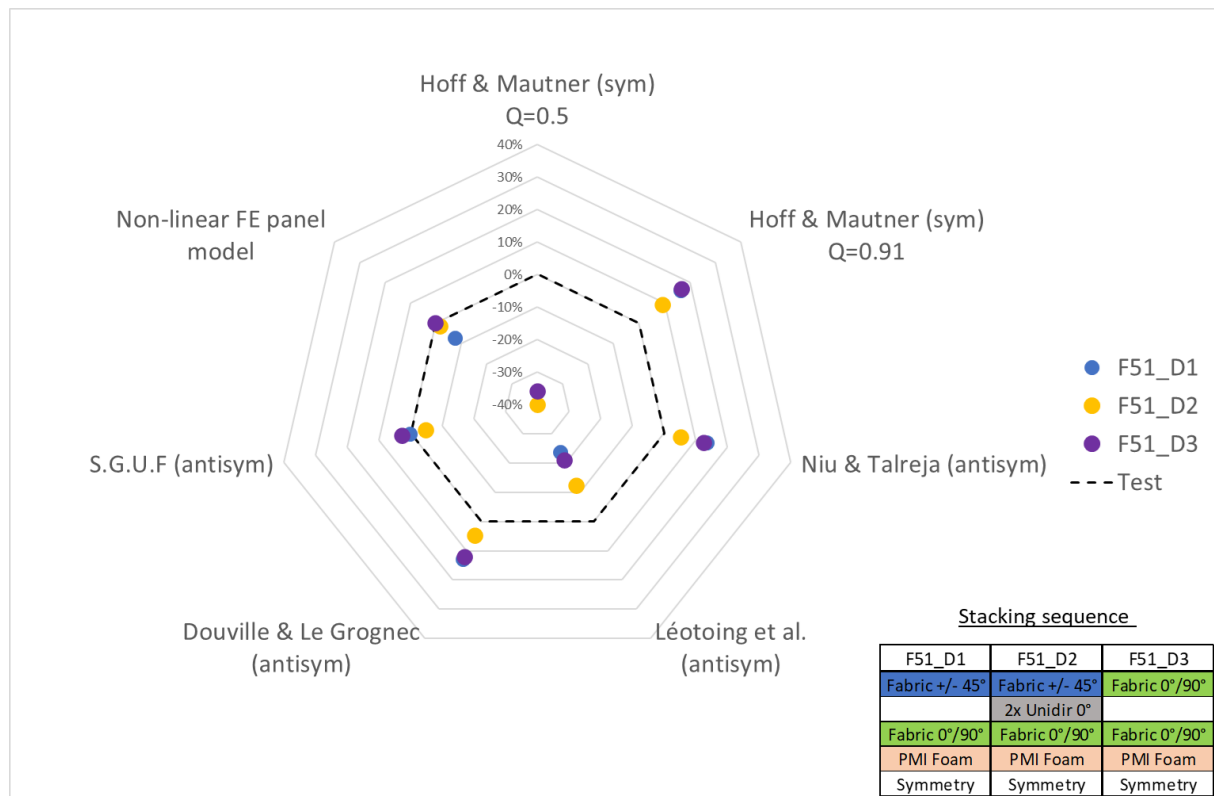


Figure 26: Radar comparison graph between models and test results.

The advanced nonlinear FE panel model provides an improved and conservative prediction of wrinkling loads over the linear models. The integration of initial imperfections in the mesh and a constitutive law for the core is effective to obtain correlation with the experimental results. Nevertheless, the failure load computed by the non-linear FE panel model is quite similar to the critical load computed by the linear S.G.U.F model. In this study, the strength issue and the stability problem are not so different. But a particular effort has been made on the quality of the specimens, where the maximum amplitude of the initial imperfections has been measured at about 10% of the thickness of the sandwiched panel (Ginot et al., 2023). In an industrial application, the imperfections may be greater and the difference between the two approaches may be significant.

6 Conclusions

An exhaustive experimental and computation dialogue on local buckling, named “wrinkling”, in sandwich panels has been performed in this paper. The test results of three sandwich panels bolted on four sides and tested in compression and shear using the VERTEX test bench have been compared to models. Stacking sequences and material properties (orthotropic asymmetric carbon skins and foam core) are in accordance with an industrial application in light aviation.

Firstly, linear 2D plane strain models are challenged with test results. Analytical formulas show optimistic correlations with test results. Beyond a framework (3D stress state; skin orthotropy; bi-modulus behaviour in the core) far from the assumptions on which they were based, these models do not take the initial imperfections into account, which can seriously lower failure loads according to the literature. For specimen F51_D3 tested in shear, the correlation is of the same order as for the specimens tested in compression. This demonstrates that models based on uniaxial loading can be used in shear.

Then an advanced non-linear Finite Elements Model of the sandwich panels has been developed. The SDIC measurement data allows the initial shape of the upper face of the sandwich panel to be directly integrated into the FE mesh. Little ripples, considered as imperfections, induce a non-linear local response generating out-of-plane displacements that affect local in-plane and out-of-plane strains. This triggers the failure of the core material. This observation leads to a refinement of the core behaviour. A constitutive law for the core is implemented in the principal directions. The law is isotropic with bi-modulus behaviour. A perfect elastoplasticity model is used for compression and an elastic response with damage

673 modelled by element deletion is used for tension. Due to convergence issues, the choice of
674 the dynamic explicit computation is made and run using the explicit solver ABAQUS. The
675 integration of initial imperfections in the mesh allows the buckling in the sandwich panel to
676 be localised. This is observed in tests. Moreover, the constitutive law for the core with failure
677 prediction (crushing and tensile failure) allows the strength approach whereas a linear
678 analytical stability approach is too optimistic (10% on average). The evolution of in-plane
679 strains in the wrinkling area with the local buckling onset is well represented in the
680 simulations.

681 The advanced non-linear FEM of the sandwich panels provides a remarkable prediction of
682 wrinkling compared to the experiment results. However, the model is the result of extensive
683 work on mesh construction, loading condition, and nonlinear material modelling with the use
684 of a dynamic explicit solver. This would not be possible without extensive instrumentation of
685 the tests and the measurement fields offered by the SDIC. In this sense, we have moved away
686 from the means and time available to the engineer for his design. Such a model would be
687 difficult to implement in an industrial context. The linear S.G.U.F model (D'Ottavio and Polit,
688 2015), which is much simpler and applicable to industrial design, also correlates well with the
689 test results. A safety approach could be used with knock down factors in the mechanical
690 characteristics of the core and/or the thickness of the skins. Both are preponderant in the
691 occurrence of wrinkling. This approach, in particular on the thickness, is widely used by the
692 industry for the calculation of buckling of shell structures by global finite element models
693 (GFEM). Similarly, Niu and Talreja, (1999) and Douville and Le Grogne, (2013) analytical
694 models can be used with a knock down factor. In general, for analytical models, the

assumptions used should be carefully checked so that the theoretical framework does not deviate too much from the real one.

Declaration of Competing Interest

The authors declare that they have no known competing financial interests or personal relationships that could have appeared to influence the work reported in this paper.

Acknowledgements

This research is part of a CIFRE PhD thesis in collaboration with the aircraft manufacturer Elixir Aircraft (<https://elixir-aircraft.com>). This work was partially funded by the “Fondation Jean-Jacques et Felicia Lopez-Loreta pour l’Excellence Académique” as part of the VIRTUOSE (VIRTual testing of aerOnautical StructurEs) project (<https://websites.isae-supaero.fr/virtuose/>). The authors gratefully acknowledge CALMIP (CALcul en MidiPyrénées, <https://calmip.univ-toulouse.fr>) for access to the HPC resources and the fast and effective computations it allows. The authors would also like to thank C3Technologies (<http://www.c3technologies.fr>) for the quality of the sandwich specimens they manufactured.

References

- Abaqus Analysis user’s manual, Dassault Systemes Simulia, V6.12. chap 11.6.1 Mass scaling. <http://193.136.142.5/v6.12/books/usb/default.htm?startat=pt04ch11s06aus74.html#usb-anl-amassscaling>
- Abrate, S., 2008. Criteria for yielding or failure of cellular materials. *J. Sandw. Struct. Mater.* 10, 5–51. <https://doi.org/10.1177/1099636207070997>
- Allen, H.G., 1969. Wrinkling and other forms of local instability, in: Neal, B.. (Ed.), *Analysis and Design of Structural Sandwich Panels*. <https://doi.org/10.1016/b978-0-08-012870-2.50012-2>
- Arbocz, J., 1982. Imperfection Data Bank, a Mean To Obtain Realistic Buckling Loads., in: Ramm, E. (Ed.), *Buckling of Shells*. pp. 535–567. <https://doi.org/10.1007/978-3-642->

720 49334-8_19

721 ASTM C297, 2004. Standard Test Method for Flexural Properties of Sandwich Constructions.

722 ASTM C365, 2011. Standard Test Method for Flatwise Compressive Properties of Sandwich
723 Cores.

724 Benson, A.S., Mayers, J., 1967. General Instability and Face Wrinkling of Sandwich Plates
725 Unified Theory and Applications. AIAA J. 5(4), 729-739. <https://doi.org/10.2514/3.4054>

726 Birman, V., Bert, C.W., 2004. Wrinkling of composite-facing sandwich panels under biaxial
727 loading. J. Sandw. Struct. Mater. 6, 217–237.
728 <https://doi.org/10.1177/1099636204033643>

729 Bisagni, C., 2000. Numerical analysis and experimental correlation of composite shell
730 buckling and post-buckling. Compos. Part B Eng. 31, 655–667.
731 [https://doi.org/10.1016/S1359-8368\(00\)00031-7](https://doi.org/10.1016/S1359-8368(00)00031-7)

732 Castanié, B., Barrau, J.J., Jaouen, J.P., 2002. Theoretical and experimental analysis of
733 asymmetric sandwich structures. Compos. Struct. 55, 295–306.
734 [https://doi.org/10.1016/S0263-8223\(01\)00156-8](https://doi.org/10.1016/S0263-8223(01)00156-8)

735 Castanié, B., Bouvet, C., Ginot, M., 2020. Review of composite sandwich structure in
736 aeronautic applications. Compos. Part C Open Access 1, 100004.
737 <https://doi.org/10.1016/j.jcomc.2020.100004>

738 D'Ottavio, M., 2016. A Sublaminar Generalized Unified Formulation for the analysis of
739 composite structures. Compos. Struct. 142, 187–199.
740 <https://doi.org/10.1016/j.compstruct.2016.01.087>

741 D'Ottavio, M., Polit, O., 2015. Linearized global and local buckling analysis of sandwich struts
742 with a refined quasi-3D model. Acta Mech. 226, 81–101.
743 <https://doi.org/10.1007/s00707-014-1169-2>

744 D'Ottavio, M., Polit, O., Ji, W., Waas, A.M., 2016. Benchmark solutions and assessment of
745 variable kinematics models for global and local buckling of sandwich struts. Compos.
746 Struct. <https://doi.org/10.1016/j.compstruct.2016.01.019>

747 Deshpande, V.S., Fleck, N.A., 2000. Isotropic constitutive models for metallic foams. J. Mech.
748 Phys. Solids 48, 1253–1283. [https://doi.org/10.1016/S0022-5096\(99\)00082-4](https://doi.org/10.1016/S0022-5096(99)00082-4)

749 Douville, M.A., Le Grogne, P., 2013. Exact analytical solutions for the local and global
750 buckling of sandwich beam-columns under various loadings. Int. J. Solids Struct. 50,
751 2597–2609. <https://doi.org/10.1016/j.ijsolstr.2013.04.013>

752 Elixir Aircraft. <https://elixir-aircraft.com>

753 Fagerberg, L., 2004. Wrinkling and compression failure transition in sandwich panels. J.
754 Sandw. Struct. Mater. 6, 129–144. <https://doi.org/10.1177/1099636204030475>

755 Fagerberg, L., Zenkert, D., 2005a. Effects of anisotropy and multiaxial loading on the
756 wrinkling of sandwich panels. J. Sandw. Struct. Mater. 7, 177–194.
757 <https://doi.org/10.1177/109963205048525>

758 Fagerberg, L., Zenkert, D., 2005b. Imperfection-induced wrinkling material failure in
759 sandwich panels. *J. Sandw. Struct. Mater.* 7, 195–219.
760 <https://doi.org/10.1177/1099636205048526>

761 Featherston, C.A., Eaton, M.J., Holford, K.M., 2012. Modelling the effects of geometric
762 imperfections on the buckling and initial post-buckling behaviour of flat plates under
763 compression using measured data. *Strain* 48, 208–215. [https://doi.org/10.1111/j.1475-](https://doi.org/10.1111/j.1475-1305.2011.00813.x)
764 [1305.2011.00813.x](https://doi.org/10.1111/j.1475-1305.2011.00813.x)

765 Gibson, L.J., Ashby, M.F., 1997. *Cellular solids*. Cambridge University Press.
766 [https://doi.org/10.1016/0021-9290\(89\)90056-0](https://doi.org/10.1016/0021-9290(89)90056-0)

767 Ginot, M., Bouvet, C., Castanié, B., Serra, J., Mahuet, N., 2023. Local buckling on large
768 sandwich panels applied to light aviation: Experimental setup and failure scenarios.
769 *Compos. Struct.* 304. <https://doi.org/10.1016/j.compstruct.2022.116439>

770 Ginot, M., D'Ottavio, M., Polit, O., Bouvet, C., Castanié, B., 2021. Benchmark of wrinkling
771 formulae and methods for pre-sizing of aircraft lightweight sandwich structures.
772 *Compos. Struct.* 273, 114387. <https://doi.org/10.1016/j.compstruct.2021.114387>

773 Hoff, N.J., Mautner, S.E., 1945. The Buckling of Sandwich-Type Panels. *J. Aeronaut. Sci.* 12,
774 285–297. <https://doi.org/10.2514/8.11246>

775 Huo, X., Jiang, Z., Luo, Q., Li, Q., Sun, G., 2022. Mechanical characterization and numerical
776 modeling on the yield and fracture behaviors of polymethacrylimide (PMI) foam
777 materials. *Int. J. Mech. Sci.* 218. <https://doi.org/10.1016/j.ijmecsci.2021.107033>

778 Kassapoglou, C., 2010. *Design and Analysis of Composites Structures*. Wiley.

779 Kassapoglou, C., Fantle, S.C., Chou, J.C., 1995. Wrinkling of composite sandwich structures
780 under compression. *J. Compos. Technol. Res.* 17, 308–316.
781 <https://doi.org/10.1520/ctr10451j>

782 Leotoing, L., 2001. *Modélisation Du Flambage Global, Local et Interactif Dans Les Structures*
783 *Sandwich En Compression*. PhD Mines de Saint-Etienne, France.
784 <https://www.theses.fr/2001EMSE0020>

785 Léotoing, L., Drapier, S., Vautrin, A., 2002. Nonlinear interaction of geometrical and material
786 properties in sandwich beam instabilities. *Int. J. Solids Struct.* 39, 3717–3739.
787 [https://doi.org/10.1016/S0020-7683\(02\)00181-6](https://doi.org/10.1016/S0020-7683(02)00181-6)

788 Ley, R.P., Lin, W., Mbanefo, U., 1999. Facesheet wrinkling in sandwich structures, NASA/CR-
789 1999-208994.
790 <https://ntrs.nasa.gov/api/citations/19990017863/downloads/19990017863.pdf>

791 Niu, K., Talreja, R., 1999. Modeling of wrinkling in sandwich panels under compression. *J.*
792 *Eng. Mech.* 125, 875–883. [https://doi.org/10.1061/\(ASCE\)0733-9399\(1999\)125:8\(875\)](https://doi.org/10.1061/(ASCE)0733-9399(1999)125:8(875))

793 Norris, C.B., 1964. Short-column compressive cf strength of sandwich constructions as
794 affected by size of cells of honeycomb core materials. *For. Prod. Lab. For. Serv. U.S.*
795 *Dep. Agric.* <https://doi.org/10.1007/BF00731082>

796 Pinho, S., 2005. Modelling composites failure laminated of using physically-based failure
 797 models. PhD Imperial College London, UK.
 798 <https://paginas.fe.up.pt/~stpinho/research/past/phd/>

799 Plantema, F. J., 1966. Sandwich Construction: The Bending and Buckling of Sandwich Beams,
 800 Plates and Shells, John Wiley and Sons.

801 Serra, J., Bouvet, C., Castanié, B., Petiot, C., 2016. Scaling effect in notched composites: The
 802 Discrete Ply Model approach. *Compos. Struct.* 148, 127–143.
 803 <https://doi.org/10.1016/j.compstruct.2016.03.062>

804 Serra, J., Pierré, J.E., Passieux, J.C., Périé, J.N., Bouvet, C., Castanié, B., 2017a. Validation and
 805 modeling of aeronautical composite structures subjected to combined loadings: The
 806 VERTEX project. Part 1: Experimental setup, FE-DIC instrumentation and procedures.
 807 *Compos. Struct.* 179, 224–244. <https://doi.org/10.1016/j.compstruct.2017.07.080>

808 Serra, J., Pierré, J.E., Passieux, J.C., Périé, J.N., Bouvet, C., Castanié, B., Petiot, C., 2017b.
 809 Validation and modeling of aeronautical composite structures subjected to combined
 810 loadings: The VERTEX project. Part 2: Load envelopes for the assessment of panels with
 811 large notches. *Compos. Struct.* 180, 550–567.
 812 <https://doi.org/10.1016/j.compstruct.2017.08.055>

813 Serra, J., Trellu, A., Bouvet, C., Rivallant, S., Castanié, B., Ratsifandrihana, L., 2021. Combined
 814 loadings after medium velocity impact on large CFRP laminated plates: Discrete ply
 815 model simulations. *Compos. Part C Open Access* 6.
 816 <https://doi.org/10.1016/j.jcomc.2021.100203>

817 Stiftinger, M.A., Rammerstorfer, F.G., 1997. Face layer Wrinkling in sandwich shells -
 818 Theoretical and experimental investigations. *Thin-Walled Struct.* 29, 113–127.

819 Sullins, R.T., Smith, G.W., Spier, E.E., 1969. Manual for structural stability analysis of
 820 sandwich plates and shells. NASA Contract. Reports CR-1457.
 821 <https://ntrs.nasa.gov/citations/19700004831>.

822 Sztefek, P., Olsson, R., 2008. Tensile stiffness distribution in impacted composite laminates
 823 determined by an inverse method. *Compos. Part A Appl. Sci. Manuf.* 39, 1282–1293.
 824 <https://doi.org/10.1016/j.compositesa.2007.10.005>

825 Thomsen, O.T., Rits, W., Eaton, D.C.G., Brown, S., 1996a. Ply drop-off effects in
 826 CFRP/honeycomb sandwich panels - Theory. *Compos. Sci. Technol.* 56, 407–422.
 827 [https://doi.org/10.1016/0266-3538\(95\)00145-X](https://doi.org/10.1016/0266-3538(95)00145-X)

828 Thomsen, O.T., Rits, W., Eaton, D.C.G., Dupont, O., Queekers, P., 1996b. Ply drop-off effects
 829 in CFRP/honeycomb sandwich panels - Experimental results. *Compos. Sci. Technol.* 56
 830 56, 423–437. [https://doi.org/https://doi.org/10.1016/0266-3538\(96\)00007-3](https://doi.org/https://doi.org/10.1016/0266-3538(96)00007-3)

831 Trellu, A., Pichon, G., Bouvet, C., Rivallant, S., Castanié, B., Serra, J., Ratsifandrihana, L., 2020.
 832 Combined loadings after medium velocity impact on large CFRP laminate plates: Tests
 833 and enhanced computation/testing dialogue. *Compos. Sci. Technol.* 196, 23.
 834 <https://doi.org/10.1016/j.compscitech.2020.108194>

835 Tuwair, H., Volz, J., ElGawady, M.A., Chandrashekhara, K., Birman, V., 2016. Modeling and
836 Analysis of GFRP Bridge Deck Panels Filled with Polyurethane Foam. *J. Bridg. Eng.* 21,
837 04016012. [https://doi.org/10.1061/\(asce\)be.1943-5592.0000849](https://doi.org/10.1061/(asce)be.1943-5592.0000849)

838 Vescovini, R., D'Ottavio, M., Dozio, L., Polit, O., 2018. Buckling and wrinkling of anisotropic
839 sandwich plates. *Int. J. Eng. Sci.* 130, 136–156.
840 <https://doi.org/10.1016/j.ijengsci.2018.05.010>

841 Vonach, W.K., Rammerstorfer, F.G., 2000. Wrinkling of thick orthotropic sandwich plates
842 under general loading conditions. *Arch. Appl. Mech.* 70, 338–348.
843 <https://doi.org/10.1007/s004199900065>

844 Wagner, H.N.R., Hühne, C., Elishakoff, I., 2020. Probabilistic and deterministic lower-bound
845 design benchmarks for cylindrical shells under axial compression. *Thin-Walled Struct.*
846 146, 106451. <https://doi.org/10.1016/j.tws.2019.106451>

847 Wang, J., Wang, H., Chen, X., Yu, Y., 2010. Experimental and numerical study of the elastic
848 properties of PMI foams. *J. Mater. Sci.* 45, 2688–2695. [https://doi.org/10.1007/s10853-](https://doi.org/10.1007/s10853-010-4250-9)
849 010-4250-9

850 Xin, R., Le, V.T., Goo, N.S., 2022. Buckling identification in composite cylindrical shells with
851 measured imperfections using a Multi-DIC method and finite element analysis. *Thin-*
852 *Walled Struct.* 177, 109436. <https://doi.org/10.1016/j.tws.2022.109436>

853 Zenkert, D., 1997. The handbook of the sandwich construction. Engineering Materials
854 Advisory Services.

855